Cell Metabolism

Article

Tumors exploit FTO-mediated regulation of glycolytic metabolism to evade immune surveillance

Graphical abstract

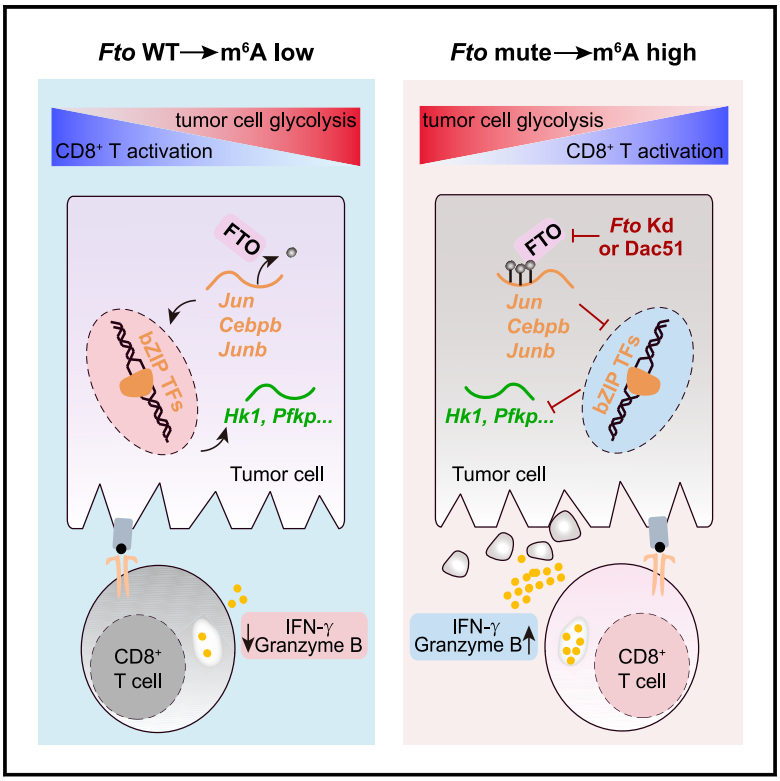

Highlights

- Tumor-intrinsic FTO restricts activation and effector states of $CD8^+$ T cells
- FTO increases glycolysis regulators JunB and C/EBPβ in an m^6A-dependent manner
- *Fto*-Kd in tumors removes the metabolic barrier for T cell activation
- The FTO inhibitor Dac51 promotes T cell response and synergizes with anti-PD-L1 blockade

Authors

Yi Liu, Guanghao Liang, Hongjiao Xu, ..., Dali Han, Cai-Guang Yang, Meng Michelle Xu

Correspondence

handl@big.ac.cn (D.H.), yangcg@simm.ac.cn (C.-G.Y.), michellexu@mail.tsinghua.edu.cn (M.M.X.)

In brief

Tumor cells utilize glycolysis to fuel rapid growth and evade immune surveillance. Liu et al. show that the m^6A demethylase FTO promotes tumor glycolysis and restricts T cell responses. Treatment with the FTO inhibitor Dac51 increases $CD8^+$ T cell infiltration in tumors and synergizes with anti-PD-L1 blockade.

Liu et al., 2021, Cell Metabolism *33*, 1–13
June 1, 2021
https://doi.org/10.1016/j.cmet.2021.04.001

CellPress

Cell Metabolism

CellPress

Article

Tumors exploit FTO-mediated regulation of glycolytic metabolism to evade immune surveillance

Yi Liu,[1,12] Guanghao Liang,[2,3,12] Hongjiao Xu,[4,5,12] Wenxin Dong,[1,12] Ze Dong,[4,5,12] Zhiwei Qiu,[1] Zihao Zhang,[1] Fangle Li,[2,3] Yue Huang,[4,5,6] Yilin Li,[1] Jun Wu,[7] Shenyi Yin,[8] Yawei Zhang,[2,3] Peijin Guo,[1] Jun Liu,[9] Jianzhong Jeff Xi,[8] Peng Jiang,[7] Dali Han,[2,3,10,11,*] Cai-Guang Yang,[4,5,6,*] and Meng Michelle Xu[1,13,*]

[1]Department of Basic Medical Sciences, School of Medicine, Institute for Immunology, Beijing Key Lab for Immunological Research on Chronic Diseases, THU-PKU Center for Life Sciences, Tsinghua University, Beijing 100084, China
[2]Key Laboratory of Genomic and Precision Medicine, Beijing Institute of Genomics, Chinese Academy of Sciences, Beijing 100101, China
[3]College of Future Technology, Sino-Danish College, University of Chinese Academy of Sciences, Beijing 100049, China
[4]State Key Laboratory of Drug Research, Shanghai Institute of Materia Medica, Chinese Academy of Sciences, Shanghai 201203, China
[5]University of Chinese Academy of Sciences, Beijing 100049, China
[6]School of Pharmaceutical Science and Technology, Hangzhou Institute for Advanced Study, University of Chinese Academy of Sciences, Hangzhou 310024, China
[7]Tsinghua-Peking Center for Life Sciences, School of Life Sciences, Tsinghua University, Beijing 100084, China
[8]State Key Laboratory of Natural and Biomimetic Drugs, Institute of Molecular Medicine, Department of Biomedical Engineering, College of Engineering, Peking University, Beijing 100871, China
[9]Department of Chemistry and Institute for Biophysical Dynamics, University of Chicago, Chicago, IL 60637, USA
[10]Institute for Stem Cell and Regeneration, Chinese Academy of Sciences, Beijing 100101, China
[11]China National Center for Bioinformation, Beijing 100101, China
[12]These authors contributed equally
[13]Lead contact
*Correspondence: handl@big.ac.cn (D.H.), yangcg@simm.ac.cn (C.-G.Y.), michellexu@mail.tsinghua.edu.cn (M.M.X.)
https://doi.org/10.1016/j.cmet.2021.04.001

SUMMARY

The ever-increasing understanding of the complexity of factors and regulatory layers that contribute to immune evasion facilitates the development of immunotherapies. However, the diversity of malignant tumors limits many known mechanisms in specific genetic and epigenetic contexts, manifesting the need to discover general driver genes. Here, we have identified the m^{6}A demethylase FTO as an essential epitranscriptomic regulator utilized by tumors to escape immune surveillance through regulation of glycolytic metabolism. We show that FTO-mediated m^{6}A demethylation in tumor cells elevates the transcription factors c-Jun, JunB, and C/EBPβ, which allows the rewiring of glycolytic metabolism. *Fto* knockdown impairs the glycolytic activity of tumor cells, which restores the function of CD8$^+$ T cells, thereby inhibiting tumor growth. Furthermore, we developed a small-molecule compound, Dac51, that can inhibit the activity of FTO, block FTO-mediated immune evasion, and synergize with checkpoint blockade for better tumor control, suggesting reprogramming RNA epitranscriptome as a potential strategy for immunotherapy.

INTRODUCTION

Emerging clinical evidence has showcased the potency of immunotherapies for controlling the progression of diverse cancers (Cohen et al., 2019; Finn et al., 2020; Schmid et al., 2020; Sharma and Allison, 2015; Wolchok et al., 2013). However, patient resistance to immunotherapy is observed frequently; such resistance can be caused by diverse factors, including oncogenic aberrance in tumor-intrinsic signaling pathways (Casey et al., 2016; Ribas and Wolchok, 2018; Sharma et al., 2017; Spranger et al., 2015; Wellenstein and de Visser, 2018). Tumor cells utilize intrinsic regulators to construct a suppressive microenvironment to evade T cell-mediated immune surveillance (Hugo et al., 2016; Riaz et al., 2017; Zelenay et al., 2015). Given the potent efficacy of immunotherapies for some patients, characterizing the genes involved in immune evasion has become a focus of intensive study.

Recent studies have suggested that immune evasion by tumor cells results from epigenomic reprogramming that reduces the extent of T cell infiltration (Loo Yau et al., 2019; Roulois et al., 2015; Sheng et al., 2018; Topper et al., 2017). CRISPR screening and transcriptome-profiling studies have identified that the PRC2 complex is responsible for silencing MHC Class I mediated-antigen presentation by depositing H3K27me3 marks in tumor cells (Burr et al., 2019). Another histone modulator, EZH2, is demonstrated to cooperate with DNMT1-mediated DNA methylation to regulate the expression of the chemokines CXCL9 and CXCL10, which consequently impedes CD8$^+$ T cell infiltration into tumors (Peng et al., 2015; Zingg et al., 2017). The epigenetic regulator PBAF complex is known to regulate the chromatin

Please cite this article in press as: Liu et al., Tumors exploit FTO-mediated regulation of glycolytic metabolism to evade immune surveillance, Cell Metabolism (2021), https://doi.org/10.1016/j.cmet.2021.04.001

accessibility of IFN-γ inducible genes, and the loss of this complex increases the sensitivity of tumor cells to T cell-mediated cytotoxicity (Pan et al., 2018). These studies collectively support a scenario wherein tumor cells achieve immune evasion at the transcriptional level via synergistic contributions from histone modifications, DNA methylation, and alteration of chromatin structure. Recently, we and others have revealed connectivity between reversible RNA m^{6}A methylation with tumorigenesis and metastasis via the dynamic alteration of m^{6}A-marked mRNA transcripts (Han et al., 2019; Jiang et al., 2017; Li et al., 2017b; Liu et al., 2018, 2019). Given the reversible nature of m^{6}A methylation, we speculate that some m^{6}A methylation programs may be initiated within tumor cells to manipulate the immune context of the tumor microenvironment. However, whether the RNA epitranscriptome is involved in immune evasion is still largely unknown.

Here, we show that FTO dominates glycolysis gene expression by preserving the basic leucine zipper (bZIP) family of transcription factors, c-Jun, JunB, and C/EBPβ, in an m^{6}A-dependent manner. Attenuating the expression or activity of FTO restrains the accumulation of these bZIP transcription factors and transcription of glycolytic-associated genes in tumor cells, which subsequently removes the metabolic barrier for T cell activation. We find that *Fto* depletion promotes the antitumor function of tumor-infiltrating T cells and inhibits tumor growth *in vivo*. Our findings uncover a metabolic role of FTO in immune evasion, and targeting its demethylase activity with the small-molecule compound Dac51 enhances the immune treatment effect of PD-L1 blockade therapy.

RESULTS

The absence of FTO inhibits tumor growth by enhancing tumor-infiltrating T cells

We initially used bulk RNA sequencing (RNA-seq) data for melanomas from The Cancer Genome Atlas (TCGA) SKCM dataset and leveraged a set of five reported genes (*CD8A*, *CD8B*, *GZMA*, *GZMB*, and *PRF1*) to define a cytotoxic T lymphocyte (CTL) score to reflect the function of tumor-infiltrating CD8$^+$ T cells (Cancer Genome Atlas Research et al., 2013; Jiang et al., 2018). This analysis indicated that patients with higher CTL scores exhibited better survival rates (Figure S1A). The CTL scores were negatively correlated with the expression of several epigenetic regulators, including the histone acetyltransferase HAT1 and the methyltransferase SUV39H2, which are reported to regulate immune evasion of tumor cells (Fan et al., 2019; Paschall et al., 2015) (Figure 1A). We noticed that FTO, an RNA demethylase (Jia et al., 2011), exhibited the most significant association with CTL scores among known epitranscriptomic regulators. In addition, the expression of *FTO* was negatively associated with the expression of *CD3D*, *GZMA*, *GZMB*, and *TNFRSF18* (Figure 1B). We then extended our analysis to include other types of cancers and found a similar negative relationship across a variety of tumors, suggesting that FTO may act in diverse tumors as an immune-inhibitory molecule for T cell functions (Figure 1C; Table S1).

To test whether the attenuation of FTO expression affects T-cell-mediated antitumor function, we used shRNA to knock down *Fto* (*Fto*-Kd) in ovalbumin (OVA)-expressing B16 melanoma (B16-OVA) cells and the lung cancer cell line LLC (Figures S1B and S1C). Quantification of the m^{6}A level in tumor cells showed that m^{6}A methylation on mRNA was elevated in the *Fto*-Kd B16-OVA and LLC cells (Figure 1D), supporting the successful knockdown of this well-characterized RNA demethylase (Wei et al., 2018). We initially compared cell growth *in vitro* and observed minimal difference in proliferation or viability between *Fto*-Kd and vector control cells (Figure S1D). We then subcutaneously (s.c.) inoculated B16-OVA and LLC cells into mice and found that the tumors developed from control cells were substantially larger than the small tumors developed from the *Fto*-Kd cells (Figures 1E and 1F). Given this apparent impact of FTO in promoting tumorigenesis, we assessed the potential role of adaptive immune responses in the observed reduction in tumor growth by s.c. injecting *Fto*-Kd tumor cells into immunodeficient Rag2$^{-/-}$ mice. We observed no difference in tumor volume between control and *Fto*-Kd tumors in these immunodeficient mice, which implicates the involvement of an adaptive immune response in the observed *Fto*-Kd-mediated disruption of tumorigenesis (Figure 1G).

To characterize the contributions of *Fto* to the tumor microenvironment, we profiled the tumor-infiltrating myeloid-derived cells (monocytes, macrophages, and dendritic cells) and T cells by flow cytometry. While the percentage of innate cells was comparable between control and *Fto*-Kd tumors, we observed significantly enhanced infiltration of CD4$^+$ and CD8$^+$ T cells in tumor tissues in the *Fto*-Kd B16-OVA and LLC tumors (Figures 1H and S1E–S1H). Further examination of antigen-specific T cell populations revealed a 2-fold increase in the frequency of tetramer$^+$ CD8$^+$ T cells in *Fto*-Kd tumors compared to control tumors (Figure 1I). We next evaluated the function of tumor-infiltrating CD8$^+$ T cells by assessing their production of IFN-γ and granzyme B. While control tumors barely generated either of these cytokines, *Fto*-Kd tumor cells had strong signals for both IFN-γ and granzyme B (Figure 1J). Moreover, the peripheral antitumor response in tumor-draining lymph nodes (tdLN) was elevated in mice bearing *Fto*-Kd cells (Figure S1I). Thus, the loss of FTO in tumors results in elevated CD8$^+$ T cell infiltration and increased CD8$^+$ T cell-mediated cytotoxicity.

Tumor-intrinsic FTO restricts the activation and effector states of CD8$^+$ T cells

Given that the initiation of cytotoxic T cell response relies on dendritic cell (DC)-mediated cross-priming (Hildner et al., 2008; Wculek et al., 2020), we assessed the cross-priming capacity of DCs isolated from the tdLNs of tumor-bearing mice. However, we found that DCs from *Fto*-Kd-cell-bearing mice exhibited a similar priming capacity compared to controls, apparently ruling out the possibility of variance in DC-mediated T cell priming (Figure S2A). We then asked whether FTO in tumor cells may directly disrupt the effector functions of T cells during TCR-mediated tumor recognition. To examine the impact of tumor-intrinsic FTO on T cells, we co-cultured B16-OVA cells and OTI CD8$^+$ T cells (whose TCR is known to react with the OVA peptide 257–264; Wick and Pfeifer, 1996). After 8 h of co-culture, we sorted OTI CD8$^+$ T cells via flow cytometry and performed RNA-seq (Figure S2B; GEO: GSE154952).

Transcriptome analysis showed that the knockdown of *Fto* in tumor cells resulted in a dramatic alteration in co-cultured

Please cite this article in press as: Liu et al., Tumors exploit FTO-mediated regulation of glycolytic metabolism to evade immune surveillance, Cell Metabolism (2021), https://doi.org/10.1016/j.cmet.2021.04.001

CellPress

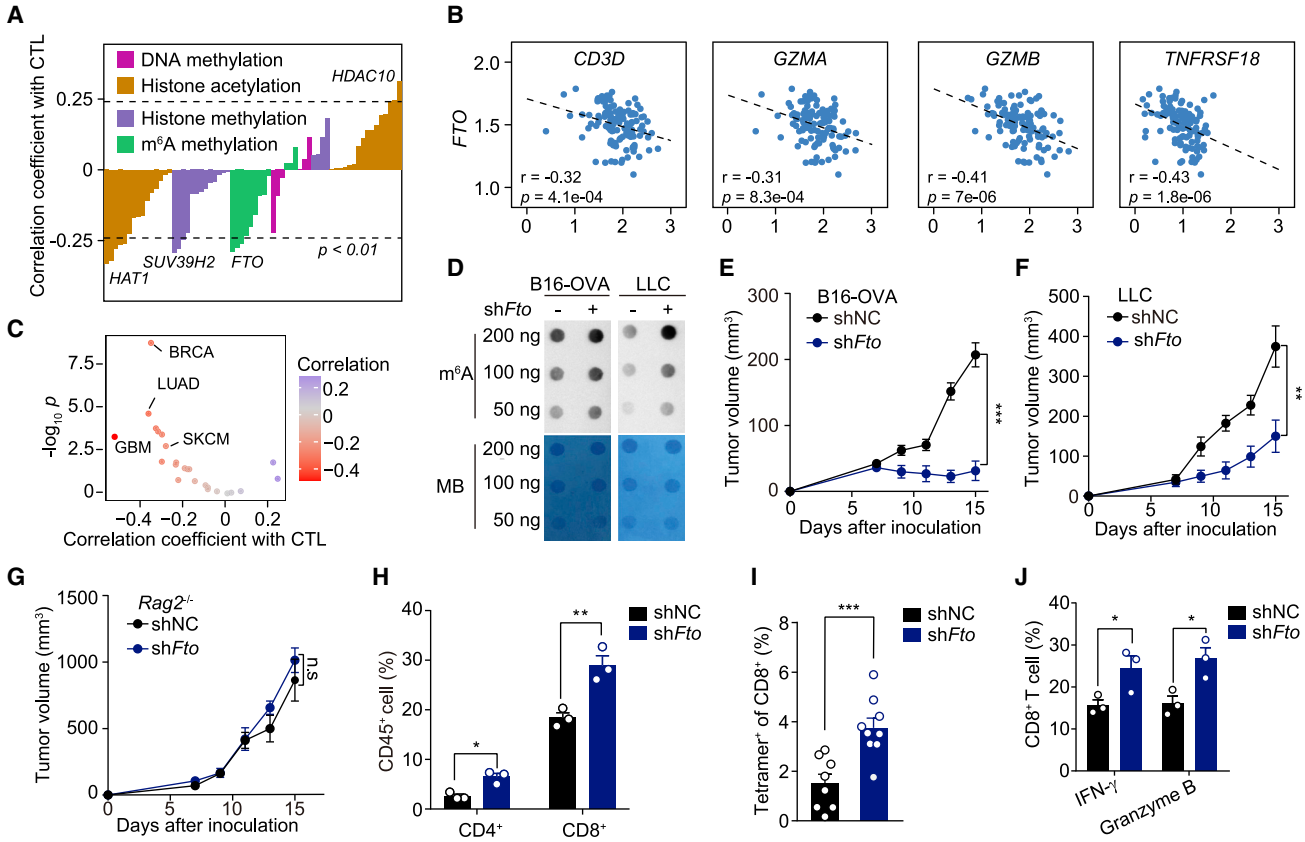

Figure 1. The absence of FTO inhibits tumor growth by enhancing tumor-infiltrating T cells

(A) Spearman correlation of the expression of known epigenetic regulators with cytotoxic T lymphocyte (CTL) scores (average expression of *CD8A*, *CD8B*, *GZMA*, *GZMB*, and *PRF1*) in 117 TCGA melanoma samples with sufficient CD8$^+$ T cell infiltration (defined as an estimated CD8$^+$ T cell infiltration level higher than upper quartile by TIMER) (STAR methods). Spearman's rho statistic is used to estimate a rank-based measure of association.

(B) Scatterplot showing the correlation of the *FTO* expression level with the expression of several activated T cell-related genes in 117 TCGA melanoma samples as in (A). The expression levels were $\log_{10}$(TPM +1). Spearman correlation coefficient (r) and p value are marked.

(C) Pan-cancer analysis of the relationship between the *FTO* expression and CTL scores in solid tumor samples with sufficient CD8$^+$ T cell infiltration. Spearman's rho statistic is used to estimate a rank-based measure of association.

(D) Dot-blot quantification of m^{6}A abundance in mRNA transcripts in B16-OVA or LLC cell lines expressing shRNA against *Fto* (sh*Fto*) or vector control (shNC); m^{6}A dot blot assay was performed with methylene blue (MB) as a loading control.

(E and F) Effect of *Fto* on tumorigenesis of B16-OVA and LLC cells in C57BL/6 mice (n = 7). 5 × 10^5 B16-OVA (E) or LLC cells (F) were s.c. inoculated into C57BL/6 mice, and tumor volume was recorded every 2 days.

(G) Effect of *Fto* on tumorigenesis of B16-OVA cells in Rag2$^{-/-}$ mice (n = 6) injected s.c. with 2 × 10^5 B16-OVA cells. Tumor volume was monitored every 2 days.

(H) FACS analysis of tumor-infiltrating CD4$^+$ and CD8$^+$ T cells (among the total CD45$^+$ population) on day 15 post tumor cell inoculation (n = 3). shNC or sh*Fto* B16-OVA cells were administrated s.c. into C57BL/6 mice.

(I) FACS analysis of tumor-infiltrating OVA-specific CD8$^+$ T cells (among the CD8$^+$ T cells) on day 15 after tumor cell inoculation (shNC, n = 8; sh*Fto*, n = 9).

(J) Quantification of IFN-γ$^+$ and granzyme B$^+$ CD8$^+$ TILs. Tumor-infiltrating T cells were re-stimulated with PMA and ionomycin for 3 h on day 9 (n = 3). IFN-γ- or granzyme-B-producing cells was determined through flow cytometry.

See also Figure S1 and Table S1.

CD8$^+$ T cells: there were 1,420 differentially upregulated genes and 1,101 downregulated genes in CD8$^+$ T cells co-cultured with *Fto*-Kd tumor cells (Figure 2A). Among the differentially expressed genes in CD8$^+$ T cells, we observed enhanced expression of cytokines and cytotoxic molecules (e.g., IL-2, IFN-γ, and granzyme B). Consistently, gene set enrichment analysis (GSEA) of CD8$^+$ T cell effector signature genes (ranking genes based on the extent of expression alteration) revealed that the T cells co-cultured with *Fto*-Kd tumor cells exhibited a more cytotoxic state than T cells co-cultured with control cells (Figure 2B). We validated the activation of T cells based on their expression of CD69 (a known marker of T cell priming) as well as the production of cytokines. Whereas co-culture with control tumor cells resulted in minimal or delayed T cell activation, rapid T cell activation was evident for cells co-cultured with *Fto*-Kd cells (Figure S2C). Specifically, the *Fto*-Kd co-cultured T cells exhibited strong production of IFN-γ and granzyme B (Figures 2C, 2D, and S2D). We also noticed that *Fto*-Kd cells were more vulnerable to T cell-mediated killing than control B16-OVA and LLC cells (Figures 2E and 2F). It should be noted that neither the expression of MHC class I molecules nor the sensitivity to IFN-γ stimuli leads to this enhanced recognition of *Fto*-Kd tumor

Please cite this article in press as: Liu et al., Tumors exploit FTO-mediated regulation of glycolytic metabolism to evade immune surveillance, Cell Metabolism (2021), https://doi.org/10.1016/j.cmet.2021.04.001

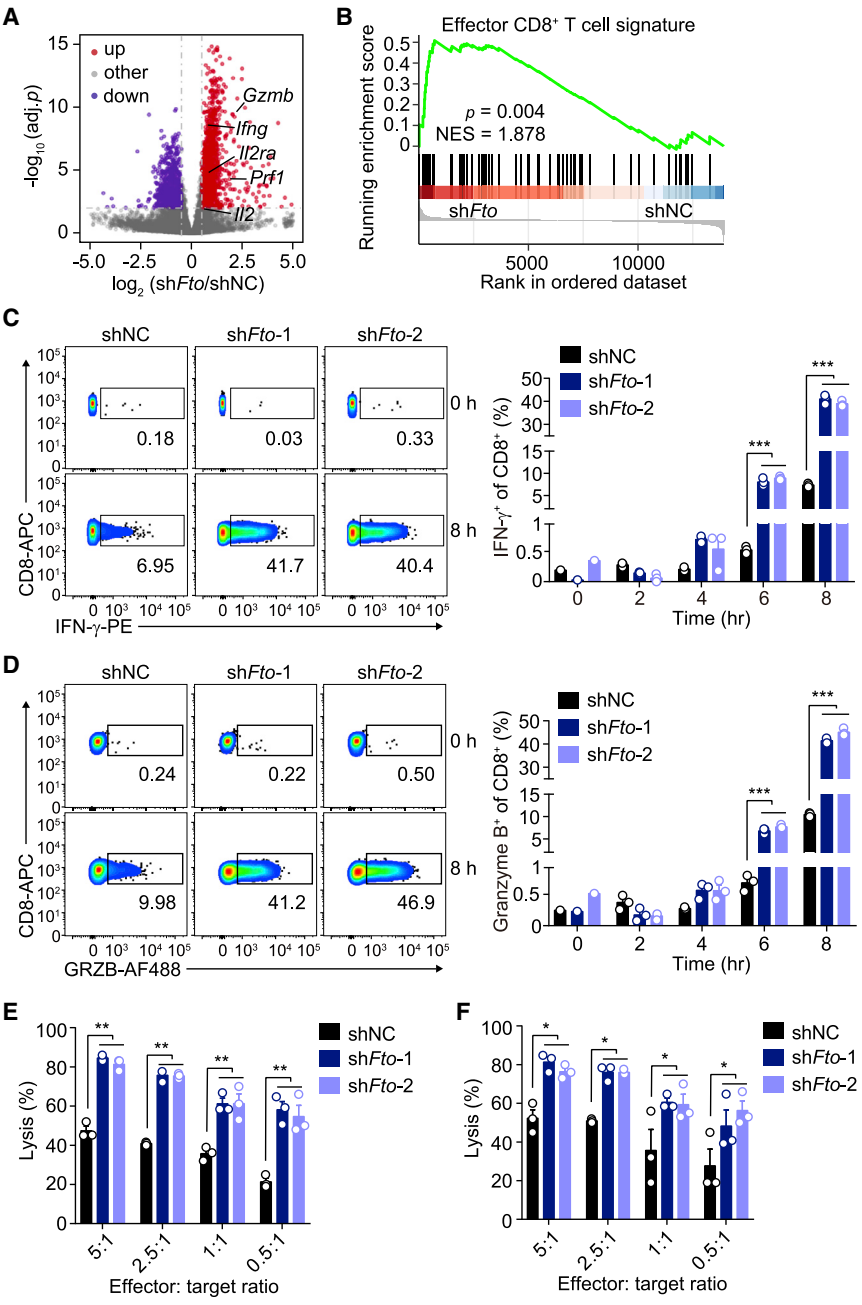

Figure 2. Tumor-intrinsic FTO restricts the activation and effector states of CD8$^+$ T cells

(A) Volcano plot of RNA-seq data for CD8$^+$ T cells co-cultured with *Fto*-Kd or control B16-OVA cells (adj.p, adjusted p value). Differentially expressed genes were defined as genes with adj.p < 0.01 and $\log_2$(fold change) more (less) than 0.5 (−0.5) (sh*Fto* versus shNC); p values were calculated with Wald test and adjusted by the Benjamini-Hochberg method.

(B) GSEA to assess specific enrichment of CD8$^+$ T cell effector signatures in CD8$^+$ T cells upon co-culture with the *Fto*-Kd or control B16-OVA cells. NES, normalized enrichment score; p value was calculated with permutation test.

(C and D) Quantification of IFN-γ (C) or granzyme B (D) production in OTI T cells after co-culture with B16-OVA cells for 0–8 h (n = 3). Naive OTI T cells were co-cultured with B16-OVA shNC/sh*Fto* cells at a ratio of 2.5:1 (T cell: B16-OVA cells).

(E and F) *In vitro* cytotoxicity assays for activated OTI T cells against *Fto*-Kd or control B16-OVA (E) or LLC cells (F) (n = 3).

See also Figure S2.

cells (Figures S2E–S2G). Taken together, these results suggest that tumor-intrinsic FTO functions as a suppressive molecule that restricts T cell activation and effector states.

Knockdown of *Fto* dampens glycolysis by repressing the expression of glycolytic transcripts

It is well established that tumors utilize glycolysis to fuel rapid growth, and the attendant consumption of glucose by tumors is known to restrict T cells metabolically, directly dampening their effector functions and thereby promoting tumor progression (Brand et al., 2016; Cascone et al., 2018; Chang et al., 2015; Renner et al., 2019). To test whether FTO somehow alters glycolytic metabolism, perhaps to the extent that limits T cell activation, we initially measured glycolytic capacity using a Seahorse instrument and found that *Fto*-Kd cells had significantly decreased glycolytic capacity compared with control B16-OVA cells (Figure 3A). To further confirm the impact of FTO on overall glycolysis activity, we cultured tumor cells with [U-$^{13}C_6$]-labeled glucose and determined the cellular levels of glycolytic intermediates with liquid chromatography-tandem mass spectrometry (LC-MS/MS). Consistent with the observation in the Seahorse assay, the levels of metabolites in glycolysis pathways were downregulated in *Fto*-Kd cells (Figure S3A). In addition, the extent of extracellular release of ^{13}C-labeled pyruvate and lactate was also significantly reduced in *Fto*-Kd cells.

To test whether reduced glycolysis in *Fto*-Kd cells is necessary for T cell activation, we treated tumor cells with oligomycin to boost their glycolysis capacity, followed by co-culturing with CD8$^+$ T cells. Compared with the untreated *Fto*-Kd, the oligomycin-treated *Fto*-Kd cells could restrict CD8$^+$ T cell activation (Figure S3B). To investigate how *Fto*-Kd dampened glycolytic metabolism in B16-OVA cells, we performed RNA-seq on *Fto*-Kd and control tumor cells. The functional enrichment analysis on differentially expressed genes revealed enrichment for glycolysis pathways among the downregulated genes in *Fto*-Kd cells (Figure 3B). We also used qPCR to confirm that genes encoding glycolysis enzymes, including *Pfkp*, *Pgam1*, and *Hk1*, were significantly downregulated upon *Fto* knockdown (Figures 3C and S3C).

Please cite this article in press as: Liu et al., Tumors exploit FTO-mediated regulation of glycolytic metabolism to evade immune surveillance, Cell Metabolism (2021), https://doi.org/10.1016/j.cmet.2021.04.001

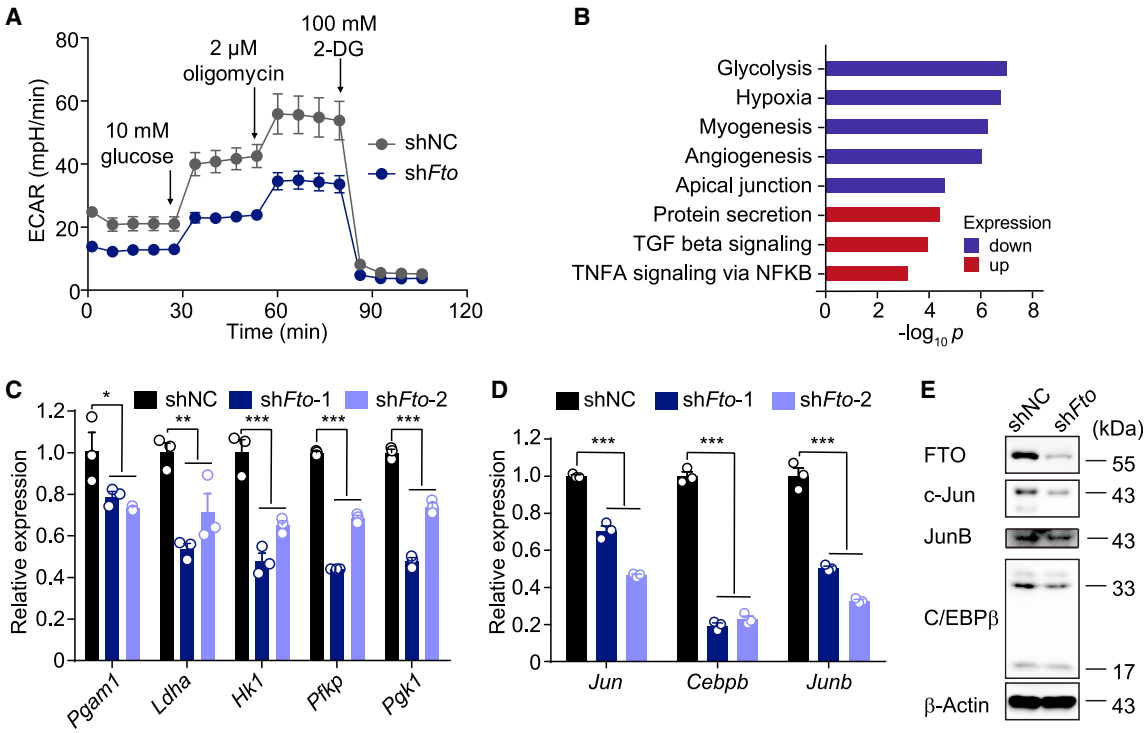

Figure 3. Knockdown of *Fto* dampens glycolysis via repressing the expression of glycolytic transcripts

(A) Glycolytic stress tests using the Seahorse XF bioanalyzer to measure the glycolytic capacity of *Fto*-Kd or control B16-OVA cells. Cells were seeded at 5,000/well in XF96 plate (n = 5).

(B) Enriched hallmark gene sets for differentially expressed genes between *Fto*-Kd and control B16-OVA cells. Differentially expressed genes were defined as genes with adj.p < 0.01 and $\log_2$(fold change) (less) than 0.5 (−0.5) (sh*Fto* versus shNC). The p value of enrichment analysis was calculated by hypergeometric distribution.

(C) qPCR analysis of mRNA levels of glycolysis-related genes after intrasample normalization to the levels of reference gene *Actb* in *Fto*-Kd or control B16-OVA cells (n = 3).

(D) qPCR analysis of *Jun*, *Cebpb*, and *Junb* mRNA levels after intrasample normalization to the levels of reference gene *Actb* in *Fto*-Kd or control B16-OVA cells (n = 3).

(E) Immunoblotting of FTO, c-Jun, JunB, C/EBPβ, and β-actin in *Fto*-Kd or control B16-OVA cells.

See also Figure S3.

Transcription factors, including those of the MYC family (c-Myc) and bZIP family, are known to transcriptionally activate genes for glycolysis enzymes (Tateishi et al., 2016). We reasoned that the downregulation of glycolysis enzymes upon *Fto*-Kd might result from the repressed expression of these transcription factors. However, c-Myc was upregulated upon *Fto*-Kd in B16-OVA cells (Figure S3D). Indeed, we found that several bZIP family transcription factors, including *Jun* (encodes c-Jun), *Cebpb* (encodes C/EBPβ), and *Junb* (encodes JunB), were all downregulated upon *Fto*-Kd, at both the RNA and protein levels (Figures 3D, 3E, and S3E). We next performed overexpression of *Junb* in tumor cells and observed that overexpression of *Junb* in *Fto*-Kd cells is sufficient to inhibit T cell activation, whereas such impaired T cell activation was markedly rescued when tumor glycolysis was blocked by 2-DG (Figure S3F). Taken together, these results suggest that enhanced T cell activation mediated by *Fto*-Kd in tumor cells might depend on the suppression of bZIP family transcription factors.

Additionally, an assay for transposase-accessible chromatin (ATAC-seq) revealed that the loci for predicted enhancers of glycolysis genes, e.g., *Ldha* and *Pfkp*, both of which have predicted binding sites of c-Jun, JunB, and C/EBPβ, were less accessible in *Fto*-Kd cells (Figure S3G). Furthermore, we noticed significantly reduced genome-wide accessibility in *Fto*-Kd cells compared with controls (Figures S3H and S3I), which were enriched with known binding motifs of the c-Jun, JunB, and C/EBPβ proteins (Figure S3J). Collectively, these results suggest that *Fto*-Kd results in glycolysis inhibition in tumor cells, likely through the transcriptional repression of glycolysis enzymes.

FTO increases multiple bZIP transcription factors, including JunB and C/EBPβ, in an m^{6}A-dependent manner

We next performed m^{6}A-seq to map the m^{6}A methylomes of B16-OVA tumor cells. In agreement with a previous report (Wei et al., 2018), *Fto*-Kd cells exhibited a moderate increase in the overall m^{6}A methylation peak number (10,811 peaks, compared with 8,479 peaks in the control cells), with especially pronounced enrichment around stop codons (Figures 4A and S4A) (Huang et al., 2019a, 2019b; Shen et al., 2020). The m^{6}A peaks of both sample groups exhibited enrichment at the canonical m^{6}A motif GGACU, as well as relatively even distributions across the

Please cite this article in press as: Liu et al., Tumors exploit FTO-mediated regulation of glycolytic metabolism to evade immune surveillance, Cell Metabolism (2021), https://doi.org/10.1016/j.cmet.2021.04.001

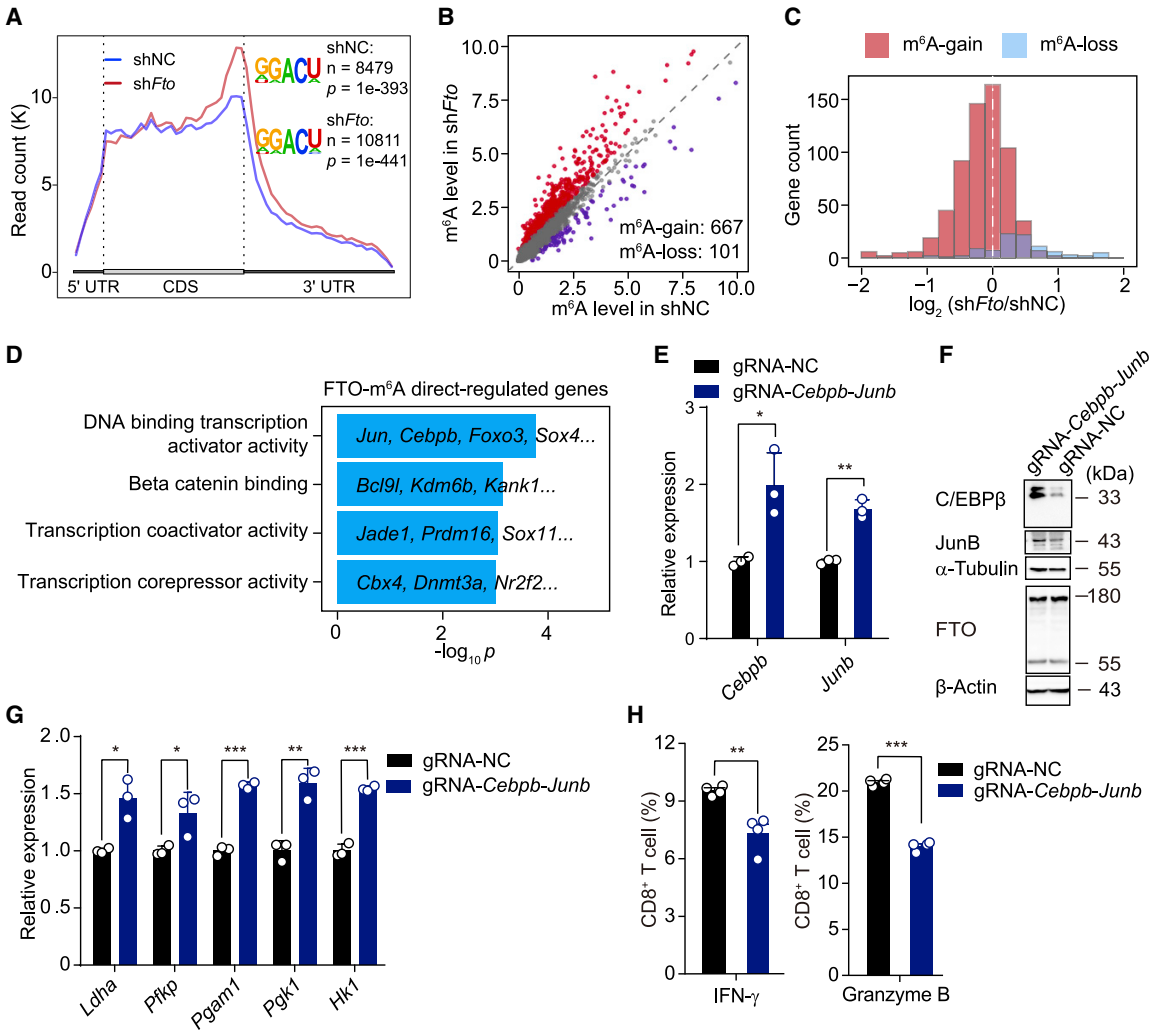

Figure 4. FTO regulates multiple bZIP transcription factors including JunB and C/EBPβ in an m^{6}A-dependent manner

(A) Metagene distribution of m^{6}A immunoprecipitation (IP) reads along the whole transcriptome (left) and enriched motifs within m^{6}A peaks called by exomePeak (right). One million reads of IP samples from each group were extracted for comparison; p values were calculated with hypergeometric test.

(B) Scatterplot showing m^{6}A methylation ratio of identified m^{6}A peaks in *Fto*-Kd or control B16-OVA cells. The m^{6}A ratio was defined as the normalized IP value divided by the expression of a given gene.

(C) Histogram of RNA-seq data for expression changes in genes exhibiting altered m^{6}A levels. The expression $\log_2$(fold change) of genes with m^{6}A-gain peaks and genes with m^{6}A-loss peaks were compared with other m^{6}A-marked genes via Mann-Whitney U test, and significant differences ($p \leq 2.2e{-}16$) were observed in both comparisons.

(D) GO term enrichment analysis for 83 identified FTO-m^{6}A direct-regulated genes. Only genes with at least 20 TPM expression, one m^{6}A-gain peak, and $\log_2$(fold change) < -0.3 were included. The p value was calculated by hypergeometric distribution.

(E–G) B16-OVA tumor cells were co-transfected with dCas13b-FTO and the tandem guide RNA plasmid targeting *Cebpb* and *Junb* for 48 h. qPCR analysis of *Cebpb*, and *Junb* mRNA levels after intra-sample normalization to the levels of reference gene *Hprt* (E). Immunoblot analysis of C/EBPβ, JunB, α-tubulin, FTO, and β-actin in B16-OVA cells (F). qPCR analysis of *Ldha*, *Pfkp*, *Pgam1*, *Pgk1*, and *Hk1* mRNA levels after intrasample normalization to the levels of reference gene *Hprt* (G) (n = 3 for E and G).

(H) Quantification of FACS analysis for IFN-γ and granzyme B production in naive OTI T cells after co-culture with B16-OVA cells for 12 h. OTI CD8$^+$ T cells were co-cultured with B16-OVA cells transfected with dCas13b-FTO and guide RNA for 48 h at a ratio of 2.5:1 (T cell: B16-OVA cell) (n = 4).

See also Figure S4.

genome. We then calculated the m^{6}A ratio for each peak and identified 667 "m^{6}A-gain peaks," comprising 86.8% of the differentially methylated m^{6}A peaks and found only 101 "m^{6}A-loss peaks" (13.2%) (Figures 4B and S4B), which revealed a global gain of m^{6}A methylation for mRNA transcripts upon *Fto* knockdown.

Since the m^{6}A level is closely associated with the decay and abundance of the m^{6}A-marked transcripts, we next focused on the expression level of the transcripts with altered m^{6}A methylation in the *Fto*-Kd samples. Indeed, inhibition of FTO was associated with a significant reduction in the expression level of genes with m^{6}A-gain peaks (Figure 4C). We then selected 83 genes with

Please cite this article in press as: Liu et al., Tumors exploit FTO-mediated regulation of glycolytic metabolism to evade immune surveillance, Cell Metabolism (2021), https://doi.org/10.1016/j.cmet.2021.04.001

downregulated expression and m^{6}A-gain peaks, which we classified as FTO-m^{6}A direct-regulated genes. By performing gene ontology analysis, we noted that this class of genes was highly enriched for predicted functions relating to DNA binding and transcriptional activation, including the bZIP family transcription factors *Jun* and *Cebpb* (Figure 4D). We evaluated the m^{6}A profiles for mRNA transcripts of all bZIP family transcriptional factors expressed in B16-OVA cells. Strikingly, 31/44 of these were marked by one or even more m^{6}A peaks (odds ratio = 2.72, p = 0.002), with 10 of them showing a significant elevation of their m^{6}A levels in *Fto*-Kd cells (odds ratio = 5.70, p = 4.57e−05). For example, *Jun* and *Cebpb* both displayed increased m^{6}A abundance at their 3′ UTRs and had decreased RNA levels (Figure S4C); recall that the aforementioned mRNA and protein data showing that *Fto*-Kd results in significantly reduced expression of *Jun*, *Cebpb*, and *Junb* (Figures 3D, 3E, and S3E). We therefore assessed whether the downregulation of *Jun*, *Junb*, and *Cebpb* in *Fto*-Kd cells is attributed to accelerated degradation rates. Indeed, *Jun*/*Junb*/*Cebpb* transcripts were degraded faster upon *Fto*-Kd (Figure S4D). Given reports of YTHDF2's function for the decay of m^{6}A-marked genes, we delivered *Ythdf2* siRNA into control cells and *Fto*-Kd cells: silencing *Ythdf2* significantly increased the expression levels of c-Jun, JunB, and C/EBPβ (Figure S4E), suggesting YTHDF2 is required for the downregulation of *Jun*/*Junb*/*Cebpb* in *Fto*-Kd cells.

To dissect whether the elevated m^{6}A abundance of these mRNA species can be attributed to the direct recognition by FTO, we overexpressed a fused CRISPR-dCas13b fusion protein with either wild-type (WT) or inactive mutant FTO in tumor cells (Figure S4F). Two gRNAs covering different sites near the m^{6}A sites were utilized, and control gRNAs (NC) targeting regions distant from any m^{6}A sites were used as a negative control (Figure S4G). We observed that targeting m^{6}A-marked loci increased the accumulation of JunB and C/EBPβ; no such upregulation was observed in assays using the inactive FTO mutant variant (Figures S4H–S4K). To further enhance the targeted demethylation, the tandem guide RNA plasmid was utilized to target m^{6}A-marked loci *of Junb* and *Cebpb* (Figure S4L). We observed that JunB and C/EBPβ, as well as downstream glycolysis genes, were significantly upregulated upon gRNA-*Cebpb*-*Junb* and dCas13b-FTO co-transfection, further verifying that FTO demethylated both *Junb* and *Cebpb* to regulate downstream glycolysis genes (Figures 4E–4G).

We next tested whether FTO somehow alters glycolytic metabolism to an extent that limits T cell activation by co-culturing naive OTI T cells with tumor cells harboring the dCas13b fusion WT FTO protein and evaluated the production of IFN-γ and granzyme B by T cells. We found that erasing the m^{6}A modification of the *Cebpb* and *Junb* transcripts through gRNA-*Cebpb*-*Junb* and dCas13b-FTO co-transfection effectively attenuated T cell activation (Figure 4H). Collectively, these results confirm that FTO is responsible for m^{6}A-dependent epitranscriptomic enhancement of *Junb* and *Cebpb* expression in tumor cells, and such enhancement promotes glycolysis in tumors and dampens T cell effector functions.

Development of Dac51 as a more potent FTO inhibitor

FTO inhibitors have been demonstrated to exhibit significant antitumor effects (Huang et al., 2019b, 2015; Huff et al., 2021; Lai et al., 2020; Su et al., 2020; Zhou and Yang, 2020). However, we are unaware of any studies exploring the use of FTO inhibitors in the immune tumor microenvironment for T cell activation. Herein, we optimized our previously reported FTO inhibitors FB23 and FB23-2, (Huang et al., 2019b), which ultimately led to the development and testing of Dac51 as a more potent FTO inhibitor (Figures 5A and S5A). *In vitro* assays showed that Dac51 exerted promising inhibitory activity on FTO demethylation activity with an IC_{50} around 0.4 μM (Figure 5B). We also determined the crystal structure of FTO in complex with Dac51 (refined to 2.35 Å resolution, PDB: 7CKK) to elucidate the molecular mechanism of FTO-Dac51 binding (Figure S5B; Table S2). Electron-density maps clearly revealed the presence of the inhibitor Dac51 (Figure S5C). In general, the FTO-Dac51 binding mode was similar to the previously characterized FTO-FB23 binding mode (Figure 5C) (Huang et al., 2019b). Additionally, extra hydrogen bonds unambiguously occur between Dac51's hydroxamic acid and Ser229; this may contribute to the substantially enhanced binding of Dac51 to FTO protein. Thus, the newly developed Dac51 is a more potent inhibitor that binds to and stabilizes FTO. We next investigated the target engagement of Dac51 in cells. In cellular thermal shift assays (CETSAs) (Martinez Molina et al., 2013), we observed that Dac51 stabilized the thermal denaturation of the FTO protein in both B16-OVA and LLC cells (Figure 5D), which indicates that FTO is a direct target of the inhibitor Dac51 in cells.

The elevated m^{6}A abundance was confirmed by dot-blot assay of the mRNA samples of Dac51-treated B16-OVA and LLC cell lines (Figure 5E). Analysis of m^{6}A-seq data of Dac51-treated/control B16-OVA cells revealed an increase of m^{6}A modification on most m^{6}A-marked genes, including *Jun* and *Cebpb* upon Dac51 treatment (Figures 5F and 5G). Consistently, we observed that Dac51 treatment caused a density-dependent reduction in *Jun*, *Cebpb*, and *Junb* at both mRNA and protein levels (Figures 5H and 5I). Similarly, Dac51 treatment and knockdown of *Fto* exhibited comparable levels of inhibition in glycolytic metabolism (Figures 5J and 5K). In summary, we have demonstrated that Dac51 could serve as a potent FTO inhibitor to dampen the glycolytic capacity of tumor cells by inhibiting FTO-mediated demethylation on transcripts including *Jun* and *Cebpb*.

Treatment with Dac51 increases T cell infiltration and synergizes with anti-PD-L1 blockade

To determine whether Dac51 exerts similar antitumor effects as *Fto* knockdown, we initially employed *in vitro* co-culture assays. Enhanced release of cytokines and elevated cytotoxic capacity were found in T cells co-cultured with Dac51-pretreated B16-OVA tumor cells (Figures 6A, 6B, and S6A). Note that we ruled out the potential impact of Dac51 on apoptosis of B16-OVA cells from these antitumor effects (Figure S6B). Also, Dac51 exhibited limited toxicity on the cells tested, including epithelial cells, fibroblasts, and T cells (Figures S6C–S6E).

We then examined the effect(s) of Dac51 on patient-derived organoids (PDOs). In line with the prior observation in the mouse model, Dac51-treated PDOs showed decreased expression levels of c-Jun, C/EBPβ, and JunB (Figure S6F). Also, genes encoded glycolysis enzymes, such as *LDHA* and *PFKP*, were also significantly downregulated upon Dac51 treatment, while T cell

Please cite this article in press as: Liu et al., Tumors exploit FTO-mediated regulation of glycolytic metabolism to evade immune surveillance, Cell Metabolism (2021), https://doi.org/10.1016/j.cmet.2021.04.001

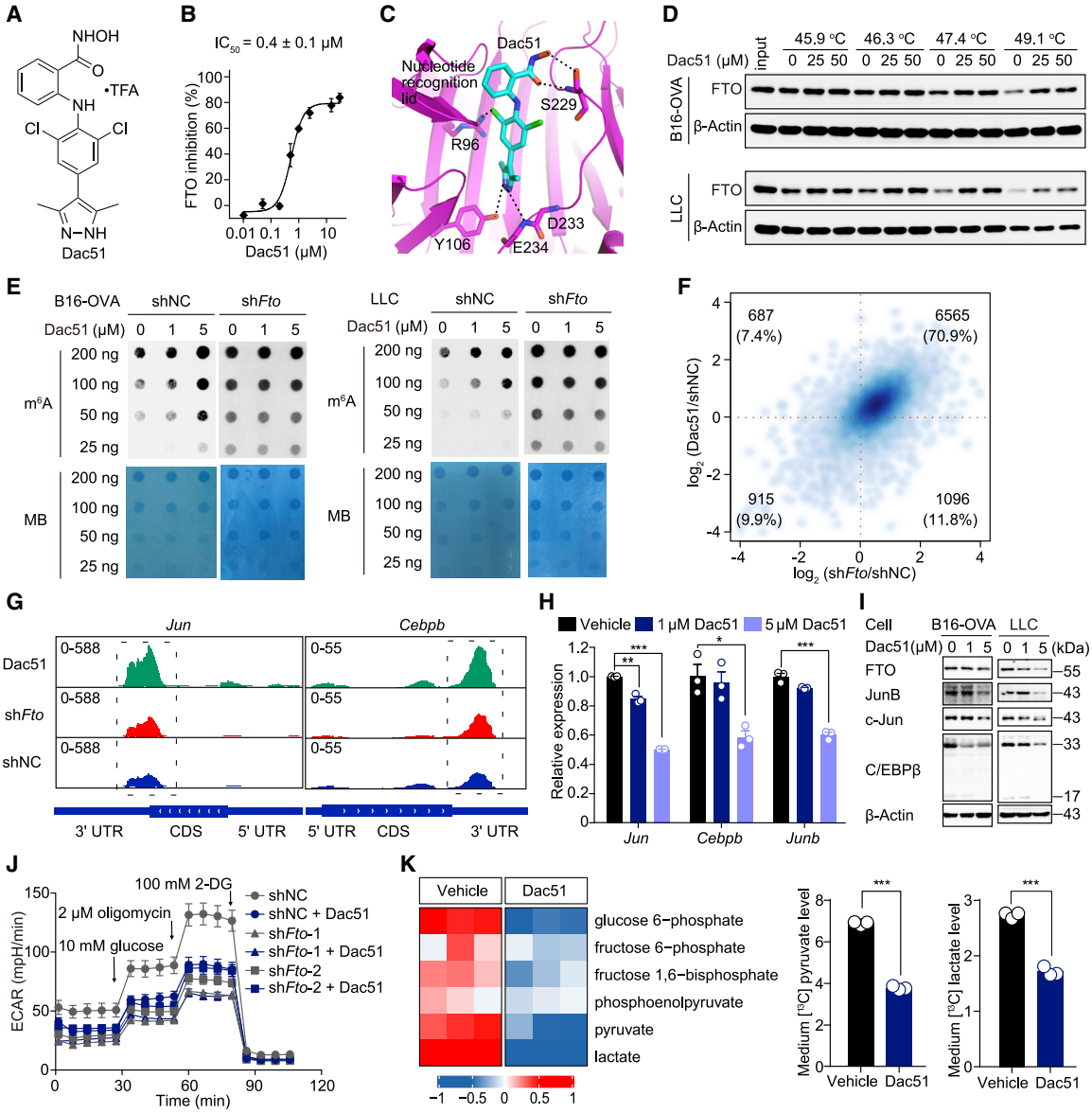

Figure 5. Characterization of the FTO inhibitor Dac51

(A) Chemical structure of Dac51.

(B) *In vitro* quantification of IC_{50} that examines the inhibitory impact of Dac51 on FTO-mediated demethylation of m^6A (n = 3).

(C) Determined crystal structural complex of FTO bound with Dac51 (2.35 Å). FTO is colored in magenta; Dca51 is in cyan. Hydrogen bonds are indicated with black dashed lines.

(D) Effect of Dac51 on the thermal denaturation of cellular FTO protein. CETSA was performed on cell lysates from B16-OVA and LLC cell lines.

(E) Effect of Dac51 on m^6A abundance in mRNA transcriptomes of B16-OVA and LLC cell lines; m^6A dot blot assays were performed with MB as the loading control.

(F) Scatterplot showing changes in the extent of m^6A methylation for shared m^6A peaks of the *Fto*-Kd and Dac51-treated groups, compared with the shNC group.

(G) IGV plot showing m^6A methylation profiles for *Jun* and *Cebpb* mRNA. The m^6A profiles of sh*Fto* and shNC groups are also shown in Figure S4C.

(H) qPCR analysis of *Jun*, *Cebpb*, and *Junb* mRNA levels after intrasample normalization to the levels of reference gene *Actb* in B16-OVA cells with or without Dac51 treatment (n = 3).

(I) Immunoblotting of FTO, JunB, c-Jun, C/EBPβ, and β-actin in B16-OVA cells and LLC cell lines with or without Dac51 treatment (1 or 5 μM).

(J) Glycolytic stress tests using a Seahorse XF bioanalyzer to measure the glycolytic capacity of B16-OVA cells with or without Dac51 treatment. Cells were seeded at 10,000/well in XF96 plate (n = 5).

(K) Heatmap shows the relative levels of downregulated glycolysis metabolites, as compared with vehicle cells. Data are represented as centered log_2-scaled value (n = 3) (left). Extracellular levels of ^{13}C-labeled pyruvate and ^{13}C-labeled lactate in the growth medium of B16-OVA cells with or without Dac51 treatment by LC-MS/MS quantitation (n = 3) (right). B16-OVA cells with or without Dac51 treatment were cultured in [U-$^{13}C_6$] glucose-supplied medium for 1 h. The relative levels of glucose-derived metabolites were determined by LC-MS/MS.

See also Figure S5 and Table S2.

Please cite this article in press as: Liu et al., Tumors exploit FTO-mediated regulation of glycolytic metabolism to evade immune surveillance, Cell Metabolism (2021), https://doi.org/10.1016/j.cmet.2021.04.001

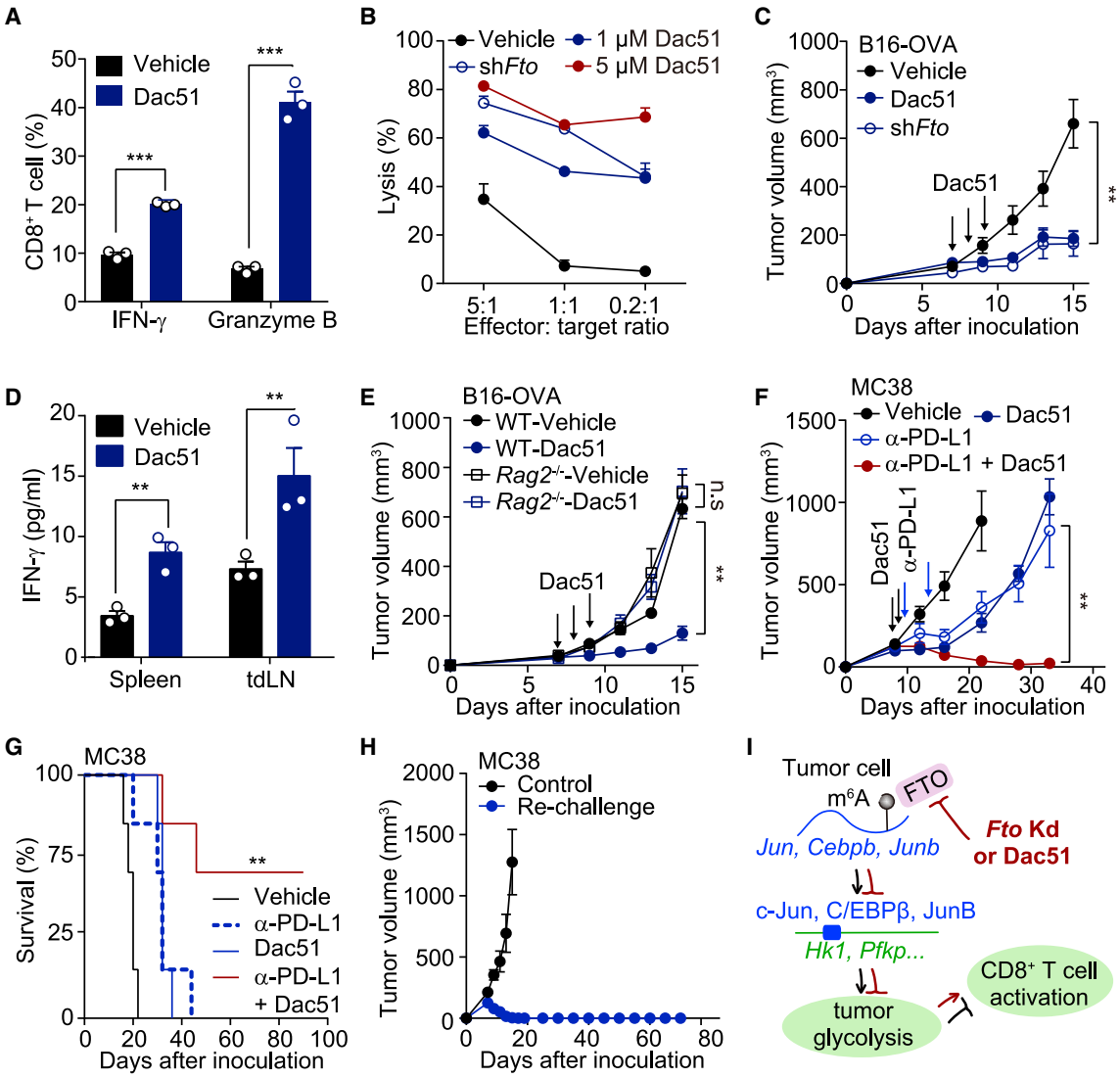

Figure 6. Treatment with Dac51 increases T cell infiltration and synergizes with anti-PD-L1 blockade

(A) Quantification of cytokine production in OTI T cells co-cultured with B16-OVA cells that were pretreated with 5 μM Dac51 for 48 h (n = 3).

(B) Effect of Dac51 on the sensitivity of B16-OVA cells to the cytotoxicity of T cells *in vitro*. shNC B16-OVA cells were pretreated with Dac51 (1 or 5 μM) for 48 h (n = 3).

(C) Effect of Dac51 on tumorigenesis of B16-OVA cells in C57BL/6 mice (n = 5). B16-OVA cells were s.c. inoculated. Tumor-bearing mice were i.p. treated with 2 mg/kg Dac51 on days 7–9.

(D) Quantification of IFN-γ production in T cells from tdLN and spleen after stimulation with synthetic OTI peptide for 16 h (n = 3).

(E) Tumorigenesis of C57BL/6 and Rag2$^{-/-}$ mice s.c. inoculated with B16-OVA cells (n = 6). Tumor-bearing mice were i.p. injected with 2 mg/kg Dac51 on days 7–9.

(F) Therapeutic effect of Dac51 on tumorigenesis of MC38 cells in C57BL/6 mice (n = 5). Mice were s.c. inoculated with 5 × 10^5 MC38 cells, and i.p. injected with 100 μg anti-PD-L1 on day 10 and 14, and/or 2 mg/kg Dac51 on days 8 and 9.

(G) Kaplan-Meier (K–M) overall survival curves for the MC38 model mice given the different therapies (n = 5).

(H) Growth curves of tumor of mice rechallenged s.c. as in (F) (survivor) (n = 3) with 5 × 10^6 MC38 cells and age-matched tumor-naive mice (control) (n = 5).

(I) Schematic model of the regulatory pathway and mechanism of FTO in tumor glycolysis and immune evasion.

See also Figure S6.

activation was consistently enhanced when co-culturing with Dac51-treated organoids (Figures S6G and S6H).

To assess the antitumor effect of Dac51 on tumor models *in vivo*, we inoculated *Fto*-Kd or control B16-OVA tumor cells into C57BL/6 mice, and treated mice daily with 2 mg/kg Dac51 starting from day 7 to day 9. Consistent with the effect of *Fto*-Kd, we observed that Dac51 treatment effectively inhibited tumor growth *in vivo* (Figure 6C). The Dac51 treatment also significantly increased the proportion of infiltrated CD8$^+$ T cells in the tumor microenvironment (Figures S6I and S6J). By monitoring T cell responses in the spleen and tdLN, we found that Dac51 treatment enhanced IFN-γ release in T cells (Figure 6D). We next examined

Please cite this article in press as: Liu et al., Tumors exploit FTO-mediated regulation of glycolytic metabolism to evade immune surveillance, Cell Metabolism (2021), https://doi.org/10.1016/j.cmet.2021.04.001

the extent to which the antitumor effect of Dac51 depends on host T cells by s.c. inoculating B16-OVA cells into Rag2$^{-/-}$ mice. There was no difference in the extent of tumor growth between the control and Dac51-treatment groups in the Rag2$^{-/-}$ model mice (Figure 6E), indicating that Dac51-mediated FTO blockade inhibits tumor growth in a T cell-dependent manner.

We also investigated whether a combinational treatment with Dac51 and an immune checkpoint blockade agent could additively improve therapeutic impacts. Compared with monotherapy groups, mice receiving the combinational therapy exhibited slower growth of B16-OVA and MC38 tumors, and their overall survival was significantly prolonged (Figures 6F, 6G, and S6K). Further examination revealed no differences in body weight among different groups, suggesting Dac51 may have limited general toxicity in mouse models (Figures S6L and S6M). To test whether combinational therapy can elicit a long-lived memory T cell response that protects mice from tumor relapse (Liu et al., 2015; Luo et al., 2017; Qiao et al., 2019), we therefore rechallenged survivor mice using 10 times more MC38 tumor cells than the initial inoculation dose, and we found complete tumor regression in rechallenged survivor mice (Figures 6H and S6N). Collectively, these *in vivo* results from multiple cancer models establish that the potent FTO inhibitor Dac51 delivers strong T cell-mediated antitumor effects and prevents tumor recurrence via memory T cell responses.

DISCUSSION

Starting from the observation that *FTO* expression is negatively correlated with cytotoxic T lymphocyte scores across multiple types of cancers, we here demonstrated that the attenuation of *Fto* expression can restrict tumor progression in an immune syngenetic mouse. We found that this antitumor response is primarily attributed to the host adaptive immune response, particularly the enhanced tumor-infiltrating CD8$^+$ T cells. We further showed that tumor-intrinsic FTO can sustain the expression of several bZIP family transcription factors such as JunB and C/EBPβ via persistently inhibiting their m^{6}A levels, which is beneficial for RNA accumulation. Thus, elevated transcription factors coordinately improve the chromatin accessibility of glycolytic-associated genes in tumor cells, which successfully established a metabolic advantage over cytotoxic CD8$^+$ T cells (Figure 6I). By developing a potent FTO inhibitor Dac51, we are able to eliminate the constraints imposed by FTO and rejuvenate T cell response, which eventually results in tumor control or complete regression upon anti-PD-L1 blockade.

A recent study demonstrated that FTO plays an oncogenic role in AML cancers: both chemical inhibition and genetic deficiency for FTO disrupted tumor progression by inhibiting LILRB4 accumulation on tumor cells (Su et al., 2020). Our study differs from previous observations from leukemia by demonstrating that attenuation of *Fto* expression reduces glycolytic activity in tumor cells, which activates antitumor T cell response. A possible explanation for this apparent discrepancy is that FTO is known to have a very large number of regulatory targets in diverse cells. That is, FTO facilitates c-Myc signaling activity in leukemia through inhibiting m^{6}A-mediated mRNA decay (Su et al., 2018), whereas our data indicate that the attenuation of *Fto* expression instead elevates c-Myc protein expression in melanoma. Another example is *LILRB4* targeted by FTO in AML is proved to promote immune evasion (Su et al., 2020). However, *LILRB4* was rarely expressed in malignant cells in the solid tumor, suggesting that AML might preferentially hijack the FTO-LILRB4 immunosuppressive axis. This result indicates an apparent diversity of FTO functions in distinct cancer types. Thus, it will likely be quite mechanistically informative to catalog the specific demethylation substrate RNA molecules of FTO across different tumor types in the future.

Since *FTO* is highly expressed on some subtypes of AML cells, the development of inhibitors targeting FTO is viewed as a promising strategy for antitumor treatment (Li et al., 2017b). Our previously developed FTO inhibitor FB23-2 was a potent inhibitor of FTO's demethylation activity, and the therapeutic utility of FB23-2 has already been demonstrated for the treatment of AML in xenotransplanted mice (Huang et al., 2019b). In the present study, we further optimized the structure of FB23-2, ultimately developing the Dac51 inhibitor, which directly binds FTO and inhibits its demethylase activity; this binding mode is clearly elucidated in the crystal structure of FTO in complex with Dac51.

Collectively, we demonstrate that Dac51 can serve as an FTO inhibitor to suppress the expression of *Jun*, *Junb*, and *Cebpb*, thereby preventing the metabolic restriction known to disrupt T cell effector functions inside tumors. It is conceivable that the combination of Dac51 with T cell function enhancers, such as checkpoint blockade agents and other immunogenic conventional therapies, could be a potent strategy to synergistically improve the adaptive immune response. Together, our study uncovers that RNA epitranscriptome can be operating as an additional layer of genetic regulation for immune evasion, which would facilitate the discovery of a new class of potentially vulnerable epitranscriptomic immunotherapy targets.

Limitations of study

Given the complexity of components in the tumor microenvironment, it is still unclear whether FTO and Dac51 also affect the glycolysis capacity and function of other tumor-infiltrating immune cells, which needs further investigation by more preclinical studies. Considering the activation of T cells also relies on glycolysis, the study on the direct effect of FTO on T cell glycolysis metabolism is limited. Even so, we have demonstrated that Dac51 does not dampen the tumor-specific T cell response, while the exact mechanism is required to be elucidated in *Fto* conditional knockout mice.

STAR★METHODS

Detailed methods are provided in the online version of this paper and include the following:

- KEY RESOURCES TABLE
- RESOURCE AVAILABILITY
  - Lead contact
  - Materials availability
  - Data and code availability
- EXPERIMENTAL MODEL AND SUBJECT DETAILS
  - Care and maintenance of mice
  - Non Small-cell Lung Carcinoma (NSCLC) organoids
  - Cell culture

SUPPLEMENTAL INFORMATION

Supplemental information can be found online at https://doi.org/10.1016/j.cmet.2021.04.001.

ACKNOWLEDGMENTS

We are grateful to Chuan He (University of Chicago) for the gift of the dCas13b-FTO vector and Jianhua Gan (Fudan University) for help in determination of FTO-Dac51 structure. We thank the Metabolomics Facility Center in the National Protein Science Technology Center of Tsinghua University for C13 isotope tracing experiments. We thank Dan Zhang and Chengpeng Jiao (Core Facility, Center of Biomedical Analysis, Tsinghua University) for technical support with confocal microscopy and Seahorse XFe96. We thank Dr. Zai Chang in the Animal Facility, Tsinghua University for his animal care support. We thank the staff from BL19U1 beamline at Shanghai Synchrotron Radiation Facility for data collection support. This work was funded by Beijing Natural Science Foundation (Z200023 to M.M.X.), Strategic Priority Research Program (XDA16010115 to D.H.), National Natural Science Foundation of China (81922054 to M.M.X., 21725801 to C.-G.Y., 31922017 and 91853132 to D.H., 21807103 to Z.D., and 21907101 to Y.H.), the National Key R&D Program of China (2016YFA0501500 to C.-G.Y. and 2018YFA0109700 to D.H.), the Key Research Program of Frontier Sciences, Chinese Academy of Sciences (ZDBS-LY-SM013 to D.H.), CAS Hundred Talent Program (to D.H.), and the Science and Technology Commission of Shanghai Municipality (18431907100 to C.-G.Y. and 18YF1428500 to Y.H.).

AUTHOR CONTRIBUTIONS

M.M.X., C.-G.Y., and D.H. conceived the project and supervised the research. Y.L. performed *in vitro* and *in vivo* experiments and performed data analysis with the help from Z.Q., Z.Z., and Y.L. Library construction, *in vivo* T cell function assay, and qPCR validation were performed by W.D.; F.L. performed library construction of ATAC-seq. J.W. performed LC-MS/MS analysis of metabolites with the instruction of P.J. J.L. and H.X. performed plasmid construction of dCas13b-FTO. H.X. characterized FTO inhibitor and contributed to the downstream gene verification with help from Y.H. Z.D. synthesized FTO inhibitor. Y.Y. generated patient-derived organoids with the instruction of J.J.X. Y.Y. and P.G. evaluated the effect of Dac51 on patient-derived organoids and performed PBMC function assay. G.L. and Y.Z. performed bioinformatics analysis. M.M.X., C.-G.Y., D.H., Y.L., G.L., H.X., W.D., and Z.D. wrote the manuscript with input from all authors. All authors discussed the results and commented on the manuscript.

DECLARATION OF INTERESTS

H.X., Z.D., Y.H., and C.-G.Y. are named inventors of pending patent applications (201810172801.4 and PCT/CN2018/077795 to the Chinese patent office) related to the work described.

Received: August 7, 2020
Revised: January 24, 2021
Accepted: April 5, 2021
Published: April 27, 2021

REFERENCES

Amemiya, H.M., Kundaje, A., and Boyle, A.P. (2019). The ENCODE blacklist: identification of problematic regions of the genome. Sci. Rep. *9*, 9354.

Brand, A., Singer, K., Koehl, G.E., Kolitzus, M., Schoenhammer, G., Thiel, A., Matos, C., Bruss, C., Klobuch, S., Peter, K., et al. (2016). LDHA-associated lactic acid production blunts tumor immunosurveillance by T and NK cells. Cell Metab. *24*, 657–671.

Broz, M.L., Binnewies, M., Boldajipour, B., Nelson, A.E., Pollack, J.L., Erle, D.J., Barczak, A., Rosenblum, M.D., Daud, A., Barber, D.L., et al. (2014). Dissecting the tumor myeloid compartment reveals rare activating antigen-presenting cells critical for T cell immunity. Cancer Cell *26*, 638–652.

Buenrostro, J.D., Giresi, P.G., Zaba, L.C., Chang, H.Y., and Greenleaf, W.J. (2013). Transposition of native chromatin for fast and sensitive epigenomic profiling of open chromatin, DNA-binding proteins and nucleosome position. Nat. Methods *10*, 1213–1218.

Burr, M.L., Sparbier, C.E., Chan, K.L., Chan, Y.C., Kersbergen, A., Lam, E.Y.N., Azidis-Yates, E., Vassiliadis, D., Bell, C.C., Gilan, O., et al. (2019). An evolutionarily conserved function of Polycomb silences the MHC Class I antigen presentation pathway and enables immune evasion in cancer. Cancer Cell *36*, 385–401.e8.

Cancer Genome Atlas Research Network, Weinstein, J.N., Collisson, E.A., Mills, G.B., Shaw, K.R., Ozenberger, B.A., Ellrott, K., Shmulevich, I., Sander, C., and Stuart, J.M. (2013). The Cancer Genome Atlas Pan-Cancer analysis project. Nat. Genet. *45*, 1113–1120.

Cascone, T., McKenzie, J.A., Mbofung, R.M., Punt, S., Wang, Z., Xu, C., Williams, L.J., Wang, Z., Bristow, C.A., Carugo, A., et al. (2018). Increased tumor glycolysis characterizes immune resistance to adoptive T cell therapy. Cell Metab. *27*, 977–987.e4.

Casey, S.C., Tong, L., Li, Y., Do, R., Walz, S., Fitzgerald, K.N., Gouw, A.M., Baylot, V., Gütgemann, I., Eilers, M., and Felsher, D.W. (2016). MYC regulates the antitumor immune response through CD47 and PD-L1. Science *352*, 227–231.

Chang, C.H., Qiu, J., O'Sullivan, D., Buck, M.D., Noguchi, T., Curtis, J.D., Chen, Q., Gindin, M., Gubin, M.M., van der Windt, G.J., et al. (2015). Metabolic competition in the tumor microenvironment is a driver of cancer progression. Cell *162*, 1229–1241.

Cohen, E.E.W., Soulières, D., Le Tourneau, C., Dinis, J., Licitra, L., Ahn, M.J., Soria, A., Machiels, J.P., Mach, N., Mehra, R., et al. (2019). Pembrolizumab versus methotrexate, docetaxel, or cetuximab for recurrent or metastatic head-and-neck squamous cell carcinoma (KEYNOTE-040): a randomised, open-label, phase 3 study. Lancet *393*, 156–167.

Colaprico, A., Silva, T.C., Olsen, C., Garofano, L., Cava, C., Garolini, D., Sabedot, T.S., Malta, T.M., Pagnotta, S.M., Castiglioni, I., et al. (2016). TCGAbiolinks: an R/Bioconductor package for integrative analysis of TCGA data. Nucleic Acids Res. *44*, e71.

Corces, M.R., Trevino, A.E., Hamilton, E.G., Greenside, P.G., Sinnott-Armstrong, N.A., Vesuna, S., Satpathy, A.T., Rubin, A.J., Montine, K.S., Wu, B., et al. (2017). An improved ATAC-seq protocol reduces background and enables interrogation of frozen tissues. Nat. Methods *14*, 959–962.

Deng, L., Liang, H., Xu, M., Yang, X., Burnette, B., Arina, A., Li, X.D., Mauceri, H., Beckett, M., Darga, T., et al. (2014). STING-dependent cytosolic DNA sensing promotes radiation-induced type I interferon-dependent antitumor immunity in immunogenic tumors. Immunity *41*, 843–852.

Dobin, A., Davis, C.A., Schlesinger, F., Drenkow, J., Zaleski, C., Jha, S., Batut, P., Chaisson, M., and Gingeras, T.R. (2013). STAR: ultrafast universal RNA-seq aligner. Bioinformatics *29*, 15–21.

Fan, P., Zhao, J., Meng, Z., Wu, H., Wang, B., Wu, H., and Jin, X. (2019). Overexpressed histone acetyltransferase 1 regulates cancer immunity by increasing programmed death-ligand 1 expression in pancreatic cancer. J. Exp. Clin. Cancer Res. *38*, 47.

Finn, R.S., Qin, S., Ikeda, M., Galle, P.R., Ducreux, M., Kim, T.Y., Kudo, M., Breder, V., Merle, P., Kaseb, A.O., et al. (2020). Atezolizumab plus bevacizumab in unresectable hepatocellular carcinoma. N. Engl. J. Med. *382*, 1894–1905.

Fulco, C.P., Nasser, J., Jones, T.R., Munson, G., Bergman, D.T., Subramanian, V., Grossman, S.R., Anyoha, R., Doughty, B.R., Patwardhan, T.A., et al. (2019). Activity-by-contact model of enhancer-promoter regulation from thousands of CRISPR perturbations. Nat. Genet. *51*, 1664–1669.

Haeussler, M., Zweig, A.S., Tyner, C., Speir, M.L., Rosenbloom, K.R., Raney, B.J., Lee, C.M., Lee, B.T., Hinrichs, A.S., Gonzalez, J.N., et al. (2019). The UCSC genome browser database: 2019 update. Nucleic Acids Res. *47*, D853–D858.

Han, D., Liu, J., Chen, C., Dong, L., Liu, Y., Chang, R., Huang, X., Liu, Y., Wang, J., Dougherty, U., et al. (2019). Anti-tumour immunity controlled through mRNA m6A methylation and YTHDF1 in dendritic cells. Nature *566*, 270–274.

Heinz, S., Benner, C., Spann, N., Bertolino, E., Lin, Y.C., Laslo, P., Cheng, J.X., Murre, C., Singh, H., and Glass, C.K. (2010). Simple combinations of lineage-determining transcription factors prime cis-regulatory elements required for macrophage and B cell identities. Mol. Cell *38*, 576–589.

Hildner, K., Edelson, B.T., Purtha, W.E., Diamond, M., Matsushita, H., Kohyama, M., Calderon, B., Schraml, B.U., Unanue, E.R., Diamond, M.S., et al. (2008). Batf3 deficiency reveals a critical role for CD8alpha+ dendritic cells in cytotoxic T cell immunity. Science *322*, 1097–1100.

Huang, Y., Yan, J., Li, Q., Li, J., Gong, S., Zhou, H., Gan, J., Jiang, H., Jia, G.F., Luo, C., and Yang, C.-G. (2015). Meclofenamic acid selectively inhibits FTO demethylation of m6A over ALKBH5. Nucleic Acids Res. *43*, 373–384.

Huang, H., Weng, H., Zhou, K., Wu, T., Zhao, B.S., Sun, M., Chen, Z., Deng, X., Xiao, G., Auer, F., et al. (2019a). Histone H3 trimethylation at lysine 36 guides m6A RNA modification co-transcriptionally. Nature *567*, 414–419.

Huang, Y., Su, R., Sheng, Y., Dong, L., Dong, Z., Xu, H., Ni, T., Zhang, Z.S., Zhang, T., Li, C., et al. (2019b). Small-molecule targeting of oncogenic FTO demethylase in acute myeloid leukemia. Cancer Cell *35*, 677–691.e10.

Huff, S., Tiwari, S.K., Gonzalez, G.M., Wang, Y., and Rana, T.M. (2021). m6A-RNA demethylase FTO inhibitors impair self-renewal in glioblastoma stem cells. ACS Chem. Biol. *16*, 324–333.

Hugo, W., Zaretsky, J.M., Sun, L., Song, C., Moreno, B.H., Hu-Lieskovan, S., Berent-Maoz, B., Pang, J., Chmielowski, B., Cherry, G., et al. (2016). Genomic and transcriptomic features of response to anti-PD-1 therapy in metastatic melanoma. Cell *165*, 35–44.

Jia, G., Fu, Y., Zhao, X., Dai, Q., Zheng, G., Yang, Y., Yi, C., Lindahl, T., Pan, T., Yang, Y.-G., and He, C. (2011). N6-methyladenosine in nuclear RNA is a major substrate of the obesity-associated FTO. Nat. Chem. Biol. *7*, 885–887.

Jiang, Q., Crews, L.A., Holm, F., and Jamieson, C.H.M. (2017). RNA editing-dependent epitranscriptome diversity in cancer stem cells. Nat. Rev. Cancer *17*, 381–392.

Jiang, P., Gu, S., Pan, D., Fu, J., Sahu, A., Hu, X., Li, Z., Traugh, N., Bu, X., Li, B., et al. (2018). Signatures of T cell dysfunction and exclusion predict cancer immunotherapy response. Nat. Med. *24*, 1550–1558.

Lai, G.-Q., Zhou, L.-L., and Yang, C.-G. (2020). RNA methylation m6A: a new code and drug target? Chin. J. Chem. *38*, 420–421.

Langmead, B., and Salzberg, S.L. (2012). Fast gapped-read alignment with Bowtie 2. Nat. Methods *9*, 357–359.

Langmead, B., Trapnell, C., Pop, M., and Salzberg, S.L. (2009). Ultrafast and memory-efficient alignment of short DNA sequences to the human genome. Genome Biol. *10*, R25.

Laurette, P., Coassolo, S., Davidson, G., Michel, I., Gambi, G., Yao, W., Sohier, P., Li, M., Mengus, G., Larue, L., and Davidson, I. (2020). Chromatin remodellers Brg1 and Bptf are required for normal gene expression and progression of oncogenic Braf-driven mouse melanoma. Cell Death Differ. *27*, 29–43.

Li, T., Fan, J., Wang, B., Traugh, N., Chen, Q., Liu, J.S., Li, B., and Liu, X.S. (2017a). TIMER: A web server for comprehensive analysis of tumor-infiltrating immune cells. Cancer Res. *77*, e108–e110.

Li, Z., Weng, H., Su, R., Weng, X., Zuo, Z., Li, C., Huang, H., Nachtergaele, S., Dong, L., Hu, C., et al. (2017b). FTO plays an oncogenic role in acute myeloid leukemia as a N6-methyladenosine RNA demethylase. Cancer Cell *31*, 127–141.

Liao, Y., Smyth, G.K., and Shi, W. (2014). featureCounts: an efficient general purpose program for assigning sequence reads to genomic features. Bioinformatics *30*, 923–930.

Liu, X., Pu, Y., Cron, K., Deng, L., Kline, J., Frazier, W.A., Xu, H., Peng, H., Fu, Y.X., and Xu, M.M. (2015). CD47 blockade triggers T cell-mediated destruction of immunogenic tumors. Nat. Med. *21*, 1209–1215.

Liu, J., Eckert, M.A., Harada, B.T., Liu, S.M., Lu, Z., Yu, K., Tienda, S.M., Chryplewicz, A., Zhu, A.C., Yang, Y., et al. (2018). m6A mRNA methylation regulates AKT activity to promote the proliferation and tumorigenicity of endometrial cancer. Nat. Cell Biol. *20*, 1074–1083.

Liu, J., Harada, B.T., and He, C. (2019). Regulation of gene expression by N6-methyladenosine in cancer. Trends Cell Biol. *29*, 487–499.

Loo Yau, H., Ettayebi, I., and De Carvalho, D.D. (2019). The cancer epigenome: exploiting its vulnerabilities for immunotherapy. Trends Cell Biol. *29*, 31–43.

Love, M.I., Huber, W., and Anders, S. (2014). Moderated estimation of fold change and dispersion for RNA-seq data with DESeq2. Genome Biol. *15*, 550.

Luo, M., Wang, H., Wang, Z., Cai, H., Lu, Z., Li, Y., Du, M., Huang, G., Wang, C., Chen, X., et al. (2017). A STING-activating nanovaccine for cancer immunotherapy. Nat. Nanotechnol. *12*, 648–654.

Martin, M. (2011). Cutadapt removes adapter sequences from high-throughput sequencing reads. EMBnet J. *17*, 10–12.

Martinez Molina, D., Jafari, R., Ignatushchenko, M., Seki, T., Larsson, E.A., Dan, C., Sreekumar, L., Cao, Y., and Nordlund, P. (2013). Monitoring drug target engagement in cells and tissues using the cellular thermal shift assay. Science *341*, 84–87.

Meng, J., Cui, X., Rao, M.K., Chen, Y., and Huang, Y. (2013). Exome-based analysis for RNA epigenome sequencing data. Bioinformatics *29*, 1565–1567.

Newman, A.M., Liu, C.L., Green, M.R., Gentles, A.J., Feng, W., Xu, Y., Hoang, C.D., Diehn, M., and Alizadeh, A.A. (2015). Robust enumeration of cell subsets from tissue expression profiles. Nat. Methods *12*, 453–457.

Oki, S., Ohta, T., Shioi, G., Hatanaka, H., Ogasawara, O., Okuda, Y., Kawaji, H., Nakaki, R., Sese, J., and Meno, C. (2018). ChIP-Atlas: a data-mining suite powered by full integration of public ChIP-seq data. EMBO Rep. *19*, e46255.

Pace, L., Goudot, C., Zueva, E., Gueguen, P., Burgdorf, N., Waterfall, J.J., Quivy, J.P., Almouzni, G., and Amigorena, S. (2018). The epigenetic control of stemness in CD8+ T cell fate commitment. Science *359*, 177–186.

Pan, D., Kobayashi, A., Jiang, P., Ferrari de Andrade, L., Tay, R.E., Luoma, A.M., Tsoucas, D., Qiu, X., Lim, K., Rao, P., et al. (2018). A major chromatin regulator determines resistance of tumor cells to T cell-mediated killing. Science *359*, 770–775.

Paschall, A.V., Yang, D., Lu, C., Choi, J.H., Li, X., Liu, F., Figueroa, M., Oberlies, N.H., Pearce, C., Bollag, W.B., et al. (2015). H3K9 trimethylation silences Fas expression to confer colon carcinoma immune escape and 5-fluorouracil chemoresistance. J. Immunol. *195*, 1868–1882.

Peng, D., Kryczek, I., Nagarsheth, N., Zhao, L., Wei, S., Wang, W., Sun, Y., Zhao, E., Vatan, L., Szeliga, W., et al. (2015). Epigenetic silencing of TH1-type chemokines shapes tumour immunity and immunotherapy. Nature *527*, 249–253.

Qiao, J., Liu, Z., Dong, C., Luan, Y., Zhang, A., Moore, C., Fu, K., Peng, J., Wang, Y., Ren, Z., et al. (2019). Targeting tumors with IL-10 prevents dendritic cell-mediated CD8+ T cell apoptosis. Cancer Cell *35*, 901–915.e4.

Ramírez, F., Dündar, F., Diehl, S., Grüning, B.A., and Manke, T. (2014). deepTools: a flexible platform for exploring deep-sequencing data. Nucleic Acids Res. *42*, W187–W191.

Rauch, S., He, C., and Dickinson, B.C. (2018). Targeted m6A reader proteins to study epitranscriptomic regulation of single RNAs. J. Am. Chem. Soc. *140*, 11974–11981.

Renner, K., Bruss, C., Schnell, A., Koehl, G., Becker, H.M., Fante, M., Menevse, A.N., Kauer, N., Blazquez, R., Hacker, L., et al. (2019). Restricting glycolysis preserves T cell effector functions and augments checkpoint therapy. Cell Rep. *29*, 135–150.e9.

Riaz, N., Havel, J.J., Makarov, V., Desrichard, A., Urba, W.J., Sims, J.S., Hodi, F.S., Martín-Algarra, S., Mandal, R., Sharfman, W.H., et al. (2017). Tumor and microenvironment evolution during immunotherapy with nivolumab. Cell *171*, 934–949.e16.

Ribas, A., and Wolchok, J.D. (2018). Cancer immunotherapy using checkpoint blockade. Science *359*, 1350–1355.

Robinson, J.T., Thorvaldsdóttir, H., Winckler, W., Guttman, M., Lander, E.S., Getz, G., and Mesirov, J.P. (2011). Integrative genomics viewer. Nat. Biotechnol. *29*, 24–26.

Ross-Innes, C.S., Stark, R., Teschendorff, A.E., Holmes, K.A., Ali, H.R., Dunning, M.J., Brown, G.D., Gojis, O., Ellis, I.O., Green, A.R., et al. (2012). Differential oestrogen receptor binding is associated with clinical outcome in breast cancer. Nature *481*, 389–393.

Roulois, D., Loo Yau, H., Singhania, R., Wang, Y., Danesh, A., Shen, S.Y., Han, H., Liang, G., Jones, P.A., Pugh, T.J., et al. (2015). DNA-demethylating agents target colorectal cancer cells by inducing viral mimicry by endogenous transcripts. Cell *162*, 961–973.

Schmid, P., Cortes, J., Pusztai, L., McArthur, H., Kümmel, S., Bergh, J., Denkert, C., Park, Y.H., Hui, R., Harbeck, N., et al. (2020). Pembrolizumab for early triple-negative breast cancer. N. Engl. J. Med. *382*, 810–821.

Sharma, P., and Allison, J.P. (2015). The future of immune checkpoint therapy. Science *348*, 56–61.

Sharma, P., Hu-Lieskovan, S., Wargo, J.A., and Ribas, A. (2017). Primary, adaptive, and acquired resistance to cancer immunotherapy. Cell *168*, 707–723.

Shen, C., Sheng, Y., Zhu, A.C., Robinson, S., Jiang, X., Dong, L., Chen, H., Su, R., Yin, Z., Li, W., et al. (2020). RNA demethylase ALKBH5 selectively promotes tumorigenesis and cancer stem cell self-renewal in acute myeloid leukemia. Cell Stem Cell *27*, 64–80.e9.

Sheng, W., LaFleur, M.W., Nguyen, T.H., Chen, S., Chakravarthy, A., Conway, J.R., Li, Y., Chen, H., Yang, H., Hsu, P.-H., et al. (2018). LSD1 ablation stimulates antitumor immunity and enables checkpoint blockade. Cell *174*, 549–563.e19.

Spranger, S., Bao, R., and Gajewski, T.F. (2015). Melanoma-intrinsic beta-catenin signalling prevents anti-tumour immunity. Nature *523*, 231–235.

Su, R., Dong, L., Li, C., Nachtergaele, S., Wunderlich, M., Qing, Y., Deng, X., Wang, Y., Weng, X., Hu, C., et al. (2018). R-2HG exhibits antitumor activity by targeting FTO/m6A/MYC/CEBPA signaling. Cell *172*, 90–105.e23.

Su, R., Dong, L., Li, Y., Gao, M., Han, L., Wunderlich, M., Deng, X., Li, H., Huang, Y., Gao, L., et al. (2020). Targeting FTO suppresses cancer stem cell maintenance and immune evasion. Cancer Cell *38*, 79–96.e11.

Subramanian, A., Tamayo, P., Mootha, V.K., Mukherjee, S., Ebert, B.L., Gillette, M.A., Paulovich, A., Pomeroy, S.L., Golub, T.R., Lander, E.S., et al. (2005). Gene set enrichment analysis: a knowledge-based approach for interpreting genome-wide expression profiles. Proc. Natl. Acad. Sci. USA *102*, 15545–15550.

Tateishi, K., Iafrate, A.J., Ho, Q., Curry, W.T., Batchelor, T.T., Flaherty, K.T., Onozato, M.L., Lelic, N., Sundaram, S., Cahill, D.P., et al. (2016). Myc-driven glycolysis is a therapeutic target in glioblastoma. Clin. Cancer Res. *22*, 4452–4465.

Topper, M.J., Vaz, M., Chiappinelli, K.B., DeStefano Shields, C.E., Niknafs, N., Yen, R.C., Wenzel, A., Hicks, J., Ballew, M., Stone, M., et al. (2017). Epigenetic therapy ties MYC depletion to reversing immune evasion and treating lung cancer. Cell *171*, 1284–1300.e21.

Wculek, S.K., Cueto, F.J., Mujal, A.M., Melero, I., Krummel, M.F., and Sancho, D. (2020). Dendritic cells in cancer immunology and immunotherapy. Nat. Rev. Immunol. *20*, 7–24.

Wei, J., Liu, F., Lu, Z., Fei, Q., Ai, Y., He, P.C., Shi, H., Cui, X., Su, R., Klungland, A., et al. (2018). Differential m6A, m6Am, and m1A demethylation mediated by FTO in the cell nucleus and cytoplasm. Mol. Cell *71*, 973–985.e5.

Wellenstein, M.D., and de Visser, K.E. (2018). Cancer-cell-intrinsic mechanisms shaping the tumor immune landscape. Immunity *48*, 399–416.

Wick, M.J., and Pfeifer, J.D. (1996). Major histocompatibility complex class I presentation of ovalbumin peptide 257–264 from exogenous sources: protein context influences the degree of TAP-independent presentation. Eur. J. Immunol. *26*, 2790–2799.

Wolchok, J.D., Kluger, H., Callahan, M.K., Postow, M.A., Rizvi, N.A., Lesokhin, A.M., Segal, N.H., Ariyan, C.E., Gordon, R.A., Reed, K., et al. (2013). Nivolumab plus ipilimumab in advanced melanoma. N. Engl. J. Med. *369*, 122–133.

Yin, S., Xi, R., Wu, A., Wang, S., Li, Y., Wang, C., Tang, L., Xia, Y., Yang, D., Li, J., et al. (2020). Patient-derived tumor-like cell clusters for drug testing in cancer therapy. Sci. Transl. Med. *12*, eaaz1723.

Yu, G., Wang, L.G., Han, Y., and He, Q.Y. (2012). clusterProfiler: an R package for comparing biological themes among gene clusters. Omics *16*, 284–287.

Zelenay, S., van der Veen, A.G., Böttcher, J.P., Snelgrove, K.J., Rogers, N., Acton, S.E., Chakravarty, P., Girotti, M.R., Marais, R., Quezada, S.A., et al. (2015). Cyclooxygenase-dependent tumor growth through evasion of immunity. Cell *162*, 1257–1270.

Zhang, Y., Liu, T., Meyer, C.A., Eeckhoute, J., Johnson, D.S., Bernstein, B.E., Nusbaum, C., Myers, R.M., Brown, M., Li, W., and Liu, X.S. (2008). Model-based analysis of ChIP-seq (MACS). Genome Biol. *9*, R137.

Zhou, L.L., and Yang, C.G. (2020). Targeting epitranscriptomic proteins for therapeutic intervention. Biochemistry *59*, 125–127.

Zhou, K.R., Liu, S., Sun, W.J., Zheng, L.L., Zhou, H., Yang, J.H., and Qu, L.H. (2017). ChIPBase v2.0: decoding transcriptional regulatory networks of non-coding RNAs and protein-coding genes from ChIP-seq data. Nucleic Acids Res. *45*, D43–D50.

Zingg, D., Arenas-Ramirez, N., Sahin, D., Rosalia, R.A., Antunes, A.T., Haeusel, J., Sommer, L., and Boyman, O. (2017). The histone methyltransferase Ezh2 controls mechanisms of adaptive resistance to tumor immunotherapy. Cell Rep. *20*, 854–867.

Please cite this article in press as: Liu et al., Tumors exploit FTO-mediated regulation of glycolytic metabolism to evade immune surveillance, Cell Metabolism (2021), https://doi.org/10.1016/j.cmet.2021.04.001

STAR★METHODS

KEY RESOURCES TABLE

REAGENT or RESOURCE	SOURCE	IDENTIFIER
Antibodies		
Anti-α-Tubulin	Proteintech	Cat#66031-1-Ig; RRID: AB_11042766
Anti-β-Actin-HRP	Santa Cruz Biotechnology	Cat#sc-47778; RRID: AB_2714189
Anti-β-Actin	Proteintech	Cat#66009-1-Ig; RRID: AB_2687938
Anti-β-Tubulin	CMCTAG	Cat#AT0003
Anti-CD4	BioLegend	Cat#100414; RRID: AB_312699
Anti-CD8	Biolegend	Cat#100712; RRID: AB_312751
Anti-CD8a	Abcam	Cat#ab22504; RRID: AB_447109
Anti-CD11b	BioLegend	Cat#101228; RRID: AB_893232
Anti-CD11c	BioLegend	Cat#117318; RRID: AB_493568
Anti-CD24	BioLegend	Cat#101831; RRID: AB_2563894
Anti-CD45	BioLegend	Cat#103138; RRID: AB_2563061
Anti-CD69	BioLegend	Cat#104522; RRID: AB_2260065
Anti-C/EBPβ	Abcam	Cat#ab15050; RRID: AB_301598
Anti-C/EBPβ	Abcam	Cat#ab32358; RRID: AB_726796
Anti-c-Jun	Cell signaling technology	Cat#9165S; RRID: AB_2130165
Anti-c-Myc	Cell signaling technology	Cat#5605; RRID: AB_1903938
Anti-F4/80	BioLegend	Cat#123116; RRID: AB_893481
Anti-FLAG	TransGen biotech	Cat#HT201-01
Anti-FTO	Abcam	Cat#ab92821; RRID: AB_10565042
Anti-GAPDH	Proteintech	Cat#60004-1-Ig; RRID: AB_2107436
Anti-Granzyme B	BioLegend	Cat#372206; RRID: AB_2687030
Anti-H-2K^b	BioLegend	Cat#116513; RRID: AB_1967103
Anti-I-A/I-E	BioLegend	Cat#107622; RRID: AB_493727
Anti-IFN-γ	BioLegend	Cat#505808; RRID: AB_315402
Anti-JunB	Cell signaling technology	Cat#3753S; RRID: AB_2130002
Anti-PD-L1	BioXCell	Cat#BE0101; RRID: AB_10949073
HRP-conjugated goat anti-rabbit IgG	Cwbio	Cat#CW0103; RRID: AB_2814709
HRP-conjugated goat anti-mouse IgG	Cwbio	Cat#CW0102; RRID: AB_2814710
Ly6C	BioLegend	Cat#128006; RRID: AB_1186135
m^{6}A antibody	abcam	Cat#ab151230; RRID: AB_2753144
Phosphorylation-specific antibodies to STAT1	Cell signaling technology	Cat#9177; RRID: AB_2197983
Rat Immunoglobulin	BioXCell	Cat#BE0094; RRID: AB_1107795
Biological samples		
Nonsmall-cell lung carcinoma (NSCLC) organoids	This paper	LL2020K060
Chemical, peptides, and recombinant proteins		
5 × sample loading buffer (Thermo Fisher)	CWBIO	Cat#CW0052S
Alkaline phosphatase	Sigma	Cat#P5931
Annexin V	Biolegend	Cat#640941
Brefeldin A	Thermo Fisher	Cat#00-4506-51
CD3	Biolegend	Cat#100359
CD28	Biolegend	Cat#102116
Collagenase D	Roche	Cat#17104-019
Dac51	This paper	N/A

(*Continued on next page*)

Please cite this article in press as: Liu et al., Tumors exploit FTO-mediated regulation of glycolytic metabolism to evade immune surveillance, Cell Metabolism (2021), https://doi.org/10.1016/j.cmet.2021.04.001

Continued

REAGENT or RESOURCE	SOURCE	IDENTIFIER
DAPI	Life technology	Cat#D1306
DNase I	Roche	Cat#10104159001
Dulbecco's modified Eagle's medium	Gibco	Cat#C11965500BT
Fetal bovine serum	Gemini	Cat#900-108
Fluoromount-G	SouthernBiotech	Cat#0100-01
HEPES	Thermo Fisher	Cat#15630080
IL-2	PEPROTECH	Cat#589104
Intracellular Staining Permeabilization Wash Buffer (10×)	Biolegend	Cat#420801
L-glutamine	Thermo Fisher	Cat#25030081
Matrigel	BD	Cat#356231
Non-essential amino acids	Thermo Fisher	Cat#11140050
NP-40	Solarbio	Cat#9016-45-9
Nuclease P1	Sigma	Cat#N8630
PBS	Solarbio	Cat#P1031
Polybrene	Sigma	Cat#TR-1003
Propidium Iodide	Biolegend	Cat#421301
protease inhibitor cocktail	Thermo Fisher	Cat#87786
puromycin	Solarbio	Cat#p8230
Streptavidin Magnetic Beads	Biolabs	Cat#S1420S
TRIzol reagent	Invitrogen	Cat#15596018
Trypan Blue	Gibco	Cat#15250061
TrypLE	Gibco	Cat#12604013
Critical commercial assays		
BCA protein assay kit	Thermo Fisher	Cat#23227
DNA Clean and Concentrator-5 Kit	Zymo	Cat#D4014
Dynabeads mRNA direct purification kit	Thermo Fisher Scientific	Cat#61002
EasyScript One-Step gDNA Removal and cDNA Synthesis SuperMix	TransGen	Cat#AE-311
EasySep Mouse CD8+ T Cell Isolation Kit	STEMCELL Technologies	Cat#19853A
EpiMark N6-methyladenosine enrichment kit	NEB	Cat#E1610S
Glucose stress fuel flex test kits	Agilent	Cat#103020
Gibson assembly master mix-assembly	NEB	Cat#E2611L
IFN-γ Flex Set CBA assay	BD	Cat#558296
iTAg Tetramer/H-2Kb-OVA (SIINFEKL)	MBL	Cat#T03000
PrimeSTAR HS DNA Polymerase	Takara	Cat#R010A
RNA Clean&Concentration-5	Zymo Research	Cat#R1016
RNA Fragmentation Reagents	Invitrogen	Cat#AM8740
RNeasy Plus Micro Kit	QIAGEN	Cat#74034
SMARTER Stranded Total RNA-seq Kit V2-Pico input	Clontech	Cat#634418
SuperSignal West Femto Maximum Sensitivity Substrate	Thermo Fisher Scientific	Cat#34096
West Dura Extended Duration Substrate kit	Thermo Fisher	Cat#34075
Deposit data		
m^6A-seq (Raw and analyzed data)	This paper	GEO: GSE154952
RNA-seq (Raw and analyzed data)	This paper	GEO: GSE154952
ATAC-seq (Raw and analyzed data)	This paper	GEO: GSE154952
Structural complex of FTO/Dac51	This paper	PDB: 7CKK

(*Continued on next page*)

Please cite this article in press as: Liu et al., Tumors exploit FTO-mediated regulation of glycolytic metabolism to evade immune surveillance, Cell Metabolism (2021), https://doi.org/10.1016/j.cmet.2021.04.001

Continued

REAGENT or RESOURCE	SOURCE	IDENTIFIER
Experimental models: cell lines		
B16-OVA	Laboratory of R.R.W.	N/A
LLC	ATCC	CRL-1642
MC38	(Deng et al., 2014)	N/A
Experimental models: organisms/strains		
C57BL/6 mouse	Charles River Laboratories	N/A
Rag2-/- mouse	Jackson Laboratory	N/A
Oligonucleotides		
5′-AUUGUCA(m^6A)CAGCAGC-3′	Genescript, China	N/A
5′-ATTGCCATTCTCGATAGG(dm6A) TCCGGTCAAACCTAGACGAA-3′	Generay, China	N/A
5′-GUAAACUUGCAGUUUAUGUAU-3′	Biosyntech, China	N/A
5′-UUCUCCGAACGUGUCACGUUU -3′	Biosyntech, China	N/A
Recombinant DNA		
pLKO.1-sh*Fto*-1	Sigma	N/A
pLKO.1-sh*Fto*-2	Sigma	N/A
pLKO.1-shNC	Sigma	N/A
Software and algorithms		
Bowtie v1.2.2	(Langmead et al., 2009)	http://bowtie-bio.sourceforge.net/index.shtml
Bowtie2 v 2.3.5	(Langmead and Salzberg, 2012)	http://bowtie-bio.sourceforge.net/bowtie2/index.shtml
FastQC v0.11.8	https://www.bioinformatics.babraham.ac.uk/projects/fastqc/	https://www.bioinformatics.babraham.ac.uk/projects/fastqc/
HOMER	(Heinz et al., 2010)	http://homer.ucsd.edu/homer/
IGV	(Robinson et al., 2011)	http://software.broadinstitute.org/software/igv/
MACS2 v2.1.3	(Zhang et al., 2008)	https://github.com/macs3-project/MACS/wiki/Install-macs2
Picard toolkit	http://broadinstitute.github.io/picard/	http://broadinstitute.github.io/picard/
Trim Galore! v 0.6.0	(Martin, 2011)	https://www.bioinformatics.babraham.ac.uk/projects/trim_galore/
Wave software	Seahorse/Agilent	https://www.agilent.com/zh-cn/product/cell-analysis/real-time-cell-metabolic-analysis/xf-software

RESOURCE AVAILABILITY

Lead contact

Further information and requests for resources and reagents should be directed to and will be fulfilled by the Lead Contact, Meng Michelle Xu (michellexu@mail.tsinghua.edu.cn).

Materials availability

All cell lines, plasmids, and other stable reagents generated in this study are available from the Lead Contact with a completed Materials Transfer Agreement.

Data and code availability

Coordinates of the FTO-Dac51 structure have been deposited in the RCSB Protein Data Bank under accession number 7CKK. The sequencing data have been deposited in Gene expression Ominibus (GEO) repository with the accession number GSE154952.

Please cite this article in press as: Liu et al., Tumors exploit FTO-mediated regulation of glycolytic metabolism to evade immune surveillance, Cell Metabolism (2021), https://doi.org/10.1016/j.cmet.2021.04.001

EXPERIMENTAL MODEL AND SUBJECT DETAILS

Care and maintenance of mice

All mice were housed under the specific pathogen-free condition. All mice were used in accordance with Tsinghua University Animal Ethics Committee guidelines. Female specific-pathogen-free C57BL/6 mice were purchased from Charles River Laboratories and female specific-pathogen-free Rag2$^{-/-}$ mice were purchased from Jackson Laboratory. Mice of ranging in age from 8-12 weeks were used for experimentation.

Non Small-cell Lung Carcinoma (NSCLC) organoids

NSCLC organoids were established from tumor cells isolated from ascites or surgery samples. Tissue samples were obtained from patients with advanced NSCLC after ethical approval (LL2020K060).

Cell culture

B16-OVA is an OVA transfected clone from mouse melanoma cell line B16-F10 (ATCC, CRL-6475) as previously described (Han et al., 2019). LLC cell line was established in the lungs of tumor-bearing C57BL/6 mice. LLC-zsGreen-OTIp (LLC-OZ) was sorted as zsGreen positive after being transfected by lentivirus expressing zsGreen-OTIp (SIINFEKL). MC38 cell line was derived from chemically induced grade III adenocarcinoma in C57BL/6 mice (Deng et al., 2014). All cell lines were verified to be mycoplasma negative. Cells were cultured in Dulbecco's modified Eagle's medium (DMEM; Gibco) supplemented with 10% heat-inactivated fetal bovine serum (FBS, Gemini), 2 mM L-glutamine (Thermo Fisher), 10 mM HEPES (Thermo Fisher), and 1% non-essential amino acids (NEAA, Thermo Fisher) at 37°C in 5% CO_2. Cell growth was monitored, and cell numbers were counted every 24 hr with Trypan Blue (Gibco) staining.

METHOD DETAILS

Lentiviral transduction of tumor cells

Lentivirus-induced *Fto*-Kd was conducted in B16-OVA and LLC cells. 3 μg PLKO.1 plasmid of shNC or sh*Fto* (Sigma), 1 μg pCMVdelta8.2 packaging vector and 1.5 μg PVSV-G enveloped vector were co-transfected into HEK-293T cells in 60 mm cell-culture dishes (NEST). After 48 and 72 hr, virus-containing supernatant was collected and filtered through a 0.45 μm PES Syringe Filter (Thermo Fisher), and then were used to infect tumor cells in the presence of 8 μg/ml Polybrene (Sigma). Finally, 5 μg/ml puromycin (Solarbio) for B16-OVA cells or 4 μg/ml puromycin for LLC cells was added to select the positive infected cells for 5 days and stable cell lines were further maintained under puromycin.

m^{6}A dot blot assay on total RNA or mRNA

The shNC/sh*Fto*-1 B16-OVA or LLC cells were cultured with indicated concentrations of Dac51 for 48 hr. Then the cells were washed with ice-cold PBS buffer and total RNA was extracted according to the instruction of TRIzol (Thermo Fisher Scientific). The concentration of total RNA sample was determined by Nanodrop 2000. Dynabeads mRNA direct purification kit (Thermo Fisher Scientific) was used for mRNA isolation from the total RNA samples. 75 μg total RNA was diluted with binding buffer (20 mM Tris-HCl (pH 7.5), 1.0 M LiCl, and 2 mM EDTA) to 100 μl and heated to 65 °C for 2 min and then immediately placed on ice for 5 min to denature. Every 75 μg total RNA was added to 1 mg beads, mixed thoroughly, and rotated for 5 min at room temperature. After that, the samples were washed by washing buffer (10 mM Tris-HCl (pH 7.5), 150 mM LiCl, and 1 mM EDTA) for three times. mRNA was eluted with 10 mM Tris-HCl (pH 7.5) by heating to 80°C for 2 min. The concentration of mRNA samples was determined by Nanodrop 2000. Indicated amounts of total RNA or mRNA samples were loaded to hybond-N+ membrane (GE Healthcare) followed by UV crosslinking for 3 min. The membrane was then blocked in 5% milk in PBST buffer for 1 hr and incubated with the m^{6}A antibody (Abcam) at 4 °C overnight. After washed with PBST buffer, the membrane was incubated with the HRP-conjugated goat anti-rabbit IgG (Cwbio) at room temperature for 1 hr, followed by PBST buffer washing. After developed with SuperSignal West Femto Maximum Sensitivity Substrate (Thermo Fisher Scientific), the loading control was established through staining of the membrane by 0.1% Methylene Blue (MB) and washed with ddH_2O until satisfying dots were obtained.

Tumor growth and treatment

When cell confluence reached 80% of the 100 mm plate, we removed the culture medium, washed the cells once with PBS, digested with 1 ml Trypsin at 37 °C for 1 min, and neutralized with 2 ml medium containing 10% FBS. After a washing step, 5 × 10^5 shNC /shFto-1 B16-OVA or LLC tumor cells were resuspended in PBS and subcutaneously injected into the flank of C57BL/6 mice. Tumor volume was measured by length (a) and width (b) and calculated as Tumor Volume = a • b^2/2. For Rag2$^{-/-}$ mice, 2 × 10^5 B16-OVA tumor cells were inoculated into the flank of mice. For Dac51 treatment, DMSO-resolved Dac51 was diluted in PBS and injected into tumor-bearing mice intraperitoneally with a dosage of 2 mg/kg for 3 consecutive days from day 7 to day 9. For anti-PD-L1 treatment, 5 × 10^5 B16-OVA or MC38 tumor cells were administrated into the flank of mice. On day 10 and day 14, a total 200 μg anti-PD-L1 (BioXCell; clone:10F.9G2) or Rat Immunoglobulin (Rat Ig) (BioXCell) were diluted in PBS before use and injected into tumor-bearing mice intraperitoneally. The bodyweight of mice was recorded on day 32. Mice with MC38 tumors smaller than 1000 mm^3 were

Please cite this article in press as: Liu et al., Tumors exploit FTO-mediated regulation of glycolytic metabolism to evade immune surveillance, Cell Metabolism (2021), https://doi.org/10.1016/j.cmet.2021.04.001

considered to be surviving. For tumor re-challenge, tumor-free mice were re-challenged with 5×10^6 MC38 tumor cells on the opposite side three months after the regression of the primary tumors. Naive mice were used as controls.

Detection of antigen-specific T cell response

spleens and tdLNs were obtained from shNC or shFto-1 B16-OVA tumor-bearing mice 15 days post tumor cell inoculation. Spleens and lymph nodes were dissected into single-cell suspensions. 5×10^5 cells were seeded and stimulated with 1 μg/ ml OTI peptide (SIINFEKL) for 72 hr in a 96-well plate. The production of IFN-γ in the supernatant was detected by Cytometric Bead Array assay (Thermo Fisher). The concentration of IFN-γ was assessed by a standard curve from flow cytometry.

Flow cytometry

Flow cytometry was performed according to the previously published paper with some modifications (Broz et al., 2014). shNC or shFto-1 B16-OVA tumor tissues were digested at 37 °C for 30 min with 1 mg/ml Collagenase D and 0.1 mg/ml DNase I (Roche). Digestion was stopped by EDTA and cells were filtrated through 70 μm cell strainers and washed twice with PBS containing 1 mM EDTA and 2% FBS (staining buffer). Cells were re-suspended in the staining buffer and stained with following antibodies on ice for 30 min: anti-CD45, anti-CD11b, anti-CD11c, anti-F4/80, Ly6C, anti-I-A/I-E, anti-CD24, anti-CD4, anti-CD8, anti-CD69, anti-H-2K^b, anti-IFN-γ and anti-Granzyme B were purchased from BioLegend. Tumor-associated macrophage 1 (TAM1, CD45$^+$Ly6C^{lo}MHCII$^+$CD24^{lo}F4/80$^+$CD11b$^+$), TAM2 (CD45$^+$Ly6C^{lo}MHCII$^+$CD24^{lo}F4/80$^+$CD11c$^+$), dendritic cells (CD45$^+$Ly6C^{lo}MHCII$^+$CD24^{hi}), monocytes (CD45$^+$CD11b$^+$Ly6C^{hi}) and neutrophils (CD45$^+$CD11b$^+$Ly6C^{int}) were determined in tumor microenvironment by flow cytometry. To detect antigen-specific T cells in tumors, samples were stained with iTAg Tetramer/H-2K^b-OVA (SIINFEKL) (MBL) for 1 hr on ice. For intracellular staining, cells were fixed with fixation buffer (Biolegend) on ice for 15 min, and then washed twice with 1 × Intracellular Staining Permeabilization Wash Buffer (10×) (Biolegend). Antibodies against IFN-γ (Clone XMG1.2) and Granzyme B (Clone: QA16A02) were added and incubated for 1 hr on ice. The cytokine producing cells were determined by flow cytometry. For assessment of apoptosis, Dac51 treated B16-OVA cells were performed Annexin V (Biolegend) and Propidium Iodide (Biolegend) staining according to the manufacturer's instructions. The apoptotic cells were then analyzed through flow cytometry. The flow cytometry data were collected on Fortessa (BD) and analyzed by FlowJo (Tree Star). For cell sorting, OTI CD8$^+$ T cells that were co-cultured with tumor cells for 6 hr were collected and washed with culture medium. Re-suspended cells were stained with anti-CD8α antibodies (Clone: 53-6.7) for 30 min on ice. After a washing step, cells were sorted on a BD FACS AriaIII (BD) and lysed in the buffer RLT plus (QIAGEN). Total RNA was extracted by RNeasy Plus Micro Kit (QIAGEN) for subsequent RNA-seq.

Tumor-infiltrating T cells *in vitro* re-stimulation

LLC shNC/sh*Fto*-1 tumor-bearing mice were sacrificed on day 9. Collected tumor tissues were digested with 1 mg/ml Collagenase D and 0.1 mg/ml DNase I (Roche) for 30 min at 37 °C. The digestion was stopped by EDTA and cells were filtered through 70 μm cell strainers. 5×10^5 cells were stimulated with Phorbol 12-Myristate 13-Acetate (PMA) (2.5 μg/ml) and ionomycin (10 μg/ml), and blocked with Brefeldin A (BFA, Thermo Fisher) for 3 hr at 37 °C. After a washing step, cells were stained with CD45 (Clone: 30-F11) and CD8 (Clone: 53-6.7) for 30 min on ice and intracellular staining was performed as described in flow cytometry.

Immunofluorescence

Tumor tissues were collected from B16-OVA or LLC shNC/sh*Fto*-1 tumor-bearing mice on day 15. Tumor tissues were embedded in OCT (Sakura 4583) and froze in – 80 °C. Tissues were cut into 8 μm pieces transversally and adhered to microscope slides (ZSGB-BIO ZLI-9506). Sections were then blocked with 5% goat serum (ZSGB-BIO) for 1 hr and incubated with antibodies directly against CD8α (KT15) at 4°C overnight in the dark. The slides were washed 3 times with PBS. 1 μg/ml DAPI (Life technology) were added and incubated for 5 min. After a final wash step, sections were mounted using the Fluoromount-G (SouthernBiotech 0100-01). Immunofluorescence was visualized utilizing a confocal microscope (ZEISS LSM880).

T cell co-culture assay

For *Fto*-Kd cells, 1×10^5 B16-OVA or LLC-OZ cells per well were seeded into the 96-well plates (NEST) with RPMI 1640 complete medium and pre-incubated for 2 hr. OTI CD8$^+$ T cells were isolated from the lymph nodes and spleens of OTI mice using EasySep Mouse CD8$^+$ T Cell Isolation Kit (STEMCELL). Purified OTI CD8$^+$ T cells were co-cultured with tumor cells at a ratio of 2.5:1 for 0-16 hr in RPMI-1640 containing 50 U/ml IL-2 (PEPROTECH), 10% FBS, 10 mM HEPES, 100 μM NEAA and 50 μM β-Mercaptoethanol. Two hr before cell collection, Brefeldin A (BFA, BioLegend, 1:1000) was added to block cytokine secretion. T cells were washed and re-suspended in staining buffer and stained with anti-CD8α (Clone: 53-6.7) and anti-CD69 (Clone: H1.2F3) antibodies for 30 min on ice. After a washing step, cells were performed intracellular staining as previously described in Flow Cytometry. For inhibitor treatment, B16-OVA cells were pre-treated with 1 μM or 5 μM Dac51 for 48 hr, and control cells were treated with DMSO. Before the co-culture was performed, pretreated tumor cells were washed twice with DMEM and re-suspended in RPMI 1640. The processes of cell co-culture and staining were following the same steps above.

T cell killing assay

2 μg/ml anti-CD3 (Biolegend) was coated to the culture dish and incubated at 4 °C overnight. Lymphocytes were obtained from lymph nodes of OTI mice. After the lymphocytes were resuspended, 0.5 μg/ml of anti-CD28 (Biolegend) was added to the anti-CD3-coated

Please cite this article in press as: Liu et al., Tumors exploit FTO-mediated regulation of glycolytic metabolism to evade immune surveillance, Cell Metabolism (2021), https://doi.org/10.1016/j.cmet.2021.04.001

culture plate for 48 hr. 1 × 10^5 B16-OVA cells were seeded into wells of a 96-well plate (NEST) with complete medium and the activated T cells were added. Dead tumor cells were counted by Trypan Blue staining after co-culture 6 hr.

T cell stimulation

Each well of 96-well plate was coated upon incubation for 12 hr in a 4°C freezer with 2 μg/ml anti-CD3 (BioLegend) in PBS. Then removing the solution and carefully washing each well with 100μl PBS, 5 × 10^5 Lymph node cells were cultured per well 100 μL 1640 completed medium containing 0.5 μg/ml anti-CD28 (BioLegend) 48 hr for stimulation.

Ex-vivo dendritic cells priming assay

$CD103^+$ dendritic cells ($B220^-$MHC $II^{hi}CD11c^+$ $CD11b^-CD103^+$) were sorted from draining lymph nodes of B16-OVA shNC/sh*Fto*-1 bearing mice on day 6 post tumor cell inoculation, and co-cultured with OTI T cells at a ratio of 1:10 for 3 days. IFN-γ production in the supernatant of medium was detected by IFN-γ Flex Set CBA assay (BD).

Seahorse XF96 respirometry

2 × 10^4 per well B16-OVA shNC/sh*Fto*-1 cells were seeded in the XF96 plate and stabilized overnight. The extracellular acidification rate (ECAR) was measured by the XF96 extracellular flux analyzer with glucose stress fuel flex test kits (Agilent). Measurements of ECAR were performed according to the manufacturer's instructions. The results were analyzed using Wave software (Seahorse/Agilent). For Seahorse analysis with Dac51 treatment, B16-OVA shNC/sh*Fto-1*/sh*Fto*-2 cells pre-treated with 5 μM Dac51 for 16 hr and then conducted ECAR as described above.

LC-MS analysis of metabolites

shNC or sh*Fto*-2 B16-OVA cells were seeded in 100 mm dishes and cultured. When cells were approximately 60%-70% density, the cells were washed twice by PBS and cultured in medium with ^{13}C-labeling glucose and 10% dialyzed FBS (Sigma) for 1 hr. Cells were collected and washed with PBS and metabolites extracted using cold 80% methanol. Then, extracts were further spun at 13,300 rpm for 10 min and collected supernatants at 4 °C. The metabolites were subjected to vacuum freeze-drying.

The Dionex Ultimate 3000 UPLC system was coupled to a TSQ Quantiva Ultra triple-quadrupole mass spectrometer (Thermo Fisher, CA), equipped with heated electrospray ionization (HESI) probe. Extracts were separated by a synergi Hydro-RP column (2.0 × 100 mm, 2.5 μm, phenomenex). A binary solvent system was used, in which mobile phase A consisted of 10 mM tributylamine adjusted with 15 mM acetic acid in water, and mobile phase B of methanol. This analysis used a 25 min gradient from 5% to 90% mobile B. Data acquired in selected reaction monitoring (SRM) for metabolites in positive-negative ion switching mode. The resolution for Q1 and Q3 are both 0.7 FWHM. The source voltage was 3500 v for positive and 2500 v for negative ion mode. The source parameters are as follows: capillary temperature: 350 °C; heater temperature: 300 °C; sheath gas flow rate: 35; auxiliary gas flow rate: 10. Tracefinder 3.2 (Thermo, USA) was applied for metabolite identification and peak integration.

RNA-seq and m^6A-seq

Total RNA was extracted from 1 × 10^6 B16-OVA cells by using TRIzol reagent (Invitrogen). For RNA-seq, 10 ng total RNA was used to construct RNA library using SMARTER Stranded Total RNA-seq Kit V2-Pico input (Clontech). For m^6A-seq, mRNA was purified with Dynabeads mRNA Purification Kit (Invitrogen). 100 ng mRNA was fragmented into ~150 nt with RNA Fragmentation Reagents (Invitrogen) at 94 °C for 45 sec. 0.5 μl of each sample was saved as input. Fragmented RNA was used for m^6A immunoprecipitation (m^6A-IP) with the EpiMark N6-methyladenosine Enrichment Kit (NEB) according to the manufacture's protocol. RNA was enriched through RNA Clean & Concentration-5 (Zymo Research) and used for library construction with SMARTer Stranded Total RNA-seq Kit V2-Pico input (Clontech).

Cytosol and nucleus separation and western blotting

For cytosol and nucleus separation, 1.5 × 10^6 shNC or sh*Fto*-1 B16-OVA cells were washed twice with ice-cold PBS (Solarbio), then re-suspended with 400 μl Cyto-Lysis Buffer (10 mM HEPES, 10 mM KCl, 0.1 mM EDTA, and 0.1 mM EGTA) containing protease inhibitor cocktail (Thermo Fisher) and incubated for 15 min on ice. We added 12.5 μl 10% NP-40 (Solarbio) into the suspension and vortexed for 15 sec, immediately followed by centrifuging at 14,000 rpm for 1 min. The supernatants were saved as cytosolic fractions. The pellets were further lysed with RIPA lysis buffer for 30 min on ice and the supernatants after centrifugation were saved as nuclear fractions. The cytosolic fractions and nuclear fractions were used for Western Blotting. For whole-cell lysate preparation, cells were lysed in RIPA lysis buffer (Invitrogen) containing protease inhibitor cocktail (Thermo Fisher) for 30 min on ice and centrifuged at 13,000 rpm for 5 min. Protein concertation of cell lysates was measured by a BCA protein assay kit (Thermo Fisher). Samples were boiled at 95 °C for 10 min with 5 × sample loading buffer (Thermo Fisher). A total of 20 μg proteins per sample were loaded into SDS-PAGE gel and transferred to PVDF membrane (Life Technologies). Membranes were blocked with TBST containing 5% non-fat dry milk for 30 min at room temperature, followed by incubation with the primary antibody overnight at 4 °C. Antibodies used in this paper were listed below: anti-FTO (Abcam), anti-c-Jun (Cell signaling technology), anti-C/EBPβ (Abcam), anti-JunB (Cell signaling technology), anti-FLAG (TransGen biotech), β-Actin antibody (Proteintech), β-Tubulin antibody (CMC-tag), anti-c-Myc (CST), anti-β-Actin-HRP (Santa Cruz Biotechnology), anti-GAPDH (Engibody), HRP-conjugated goat anti-rabbit IgG (Cwbio) and HRP-conjugated goat anti-mouse IgG (Cwbio). Phosphorylation-specific antibody to STAT1 was from Cell Signaling Technology. Then, the

Please cite this article in press as: Liu et al., Tumors exploit FTO-mediated regulation of glycolytic metabolism to evade immune surveillance, Cell Metabolism (2021), https://doi.org/10.1016/j.cmet.2021.04.001

membranes were washed with TBST and incubated with diluted HRP-conjugated secondary antibodies for 1 hr at room temperature. HRP signals were detected using West Dura Extended Duration Substrate kit (Thermo Fisher) and visualized with a Minichemi 610 chemiluminescent imager (Sagecreation).

RT-qPCR

Total RNA from tumor cells was extracted using TRIzol reagent and cDNA was synthesized using EasyScript One-Step gDNA Removal and cDNA Synthesis SuperMix (TransGen). RT qPCR was performed using TransStart Top Green qPCR SuperMix (TransGen) on the StepOnePlus system (ABI). The qPCR conditions were 94 °C for 30 sec; followed by 40 cycles of 94 °C for 5 sec and 60 °C for 31 sec. Amplification of specific transcripts was confirmed by melting curve profiles generated at the end of the PCR program. Expression levels of target genes were normalized to the expression of the *Actb* or *Hprt* gene and were calculated based on the comparative cycle threshold method ($2^{-\Delta\Delta Ct}$).

ATAC-seq

Omni-ATAC was performed according to a previous protocol with some modifications (Corces et al., 2017). 5×10^4 viable shNC or sh*Fto*-1 B16-OVA cells were collected and pelleted for each sample. The permeabilization was performed by adding 50 μl cold ATAC-Resuspension Buffer (RSB, 10 mM Tris-HCl (pH 7.5), 10 mM NaCl, 3 mM $MgCl_2$) containing 0.1% NP40, 0.1% Tween-20, 0.01% digitonin and incubated on ice for 3 min. After stopping the reaction by adding 1 ml cold ATAC-RSB containing 0.1% Tween-20, each cell pellet was resuspended in 50 μl transposition mixture [25 μl 2 × TD buffer (20 mM Tris-HCl (pH 7.5), 10 mM $MgCl_2$, 20% Dimethyl Formamide), 2.5 μl transposase (100 nM final), 16.5 μl PBS, 0.5 μl 1% digitonin, 0.5 μl 10% Tween-20, 5 μl H_2O] and incubated at 37 °C for 30 min in a thermomixer with 1000 rpm mixing. The samples were cleanup with DNA Clean and Concentrator-5 Kit (Zymo). DNAs were eluted in 22 μl nuclease free water. The 5-cycle pre-amplification were performed in the following 50 μl system: 25 μM Primer N502 2.5 μl, 25 μM Primer N70X 2.5 μl (see Illumina Nextera Transposase Adapters), Q5 High-Fidelity 2 × Master Mix (NEB, M0492S) 25 μl, and transposed sample 20 μl. Then qPCR was performed to determine additional cycles. The qPCR system (10 μl) was: nuclease free water 1.2 μl, 25 μM Primer N502 0.25 μl, 25 μM Primer N70X 0.25 μl, 2 × TransStart Top Green qPCR SuperMix (TransGen) 5 μl and pre-amplified sample 3.3 μl. Then the remainder of the pre-amplified DNA was used to run the required number of additional cycles (5-6 cycles). Finally, the samples were purified twice with 1.2 × Agencourt AMPure XP (Beckman Coulter). The libraries were sequenced on Illumina HiSeqX10 platform with paired-end 150 bp mode.

dCas13b-FTO system

The original dCas13b-FTO plasmid was a gift from Chuan He, and the generation of dCas13b-FTO-gRNA plasmids was according to previously published procedures (Rauch et al., 2018). FTO binding sites of transcription factors and m^6A modification sites were obtained through our previous bioinformatic data analysis. The fragments of the dCas13b-gRNA plasmids were generated with the primers listed in Table S3 and PrimeSTAR HS DNA Polymerase (Takara) and then assembled by Gibson assembly master mix-assembly (NEB). The sequences of the dCas13b-gRNA plasmids were verified by the double digests and further sequenced by ShangHai MAP Biotech B16-OVA cells were plated in 6-well plates (NEST) and transfected with 3.9 μg dCas13b-FTO wt/mutant and 3 μg gRNA plasmids for 48 hr. Subsequently, the cells were washed with 1 × PBS and subjected for RT-qPCR analysis with the primers listed in Table S3 and western blot assay with the FTO antibody (Abcam), c-Jun antibody (Cell signaling technology, 9165S), C/EBPβ antibody (Abcam), JUNB antibody (Cell signaling technology), FLAG antibody (TransGen biotech), β-Tubulin antibody (CMC-tag), β-Actin antibody (Proteintech), HRP-conjugated goat anti-rabbit IgG (Cwbio) and HRP-conjugated goat anti-mouse IgG (Cwbio). For co-culture assay, B16-OVA cells transfected with dCas13b-FTO and guide RNA were co-cultured with purified OTI $CD8^+$ T cells for 8 hr following the previously described procedures.

4sU labelling and mRNA stability

The 100 mm plate of shNC or sh*Fto*-1 B16-OVA cells were treated with 500 μM 4sU at 70% confluency. Cells were harvested at different time intervals (15 and 30 min after treatment). To biotinylate the 4sU labeled RNA, 25 μg total RNA was incubated with 50 μg HPDP-Biotin in biotinylation buffer for 3 hr. The biotinylated RNA was purified from the excess of HPDP-Biotin using phenol-chloroform-isoamyl alcohol. RNA was precipitated with 1/10 volume of 5 M NaCl and an equal volume of isopropanol then centrifuged at 20,000 × g for 20 min. The pellet was washed with 500 μl 80% ethanol and dissolved in 20 μl RNase-free water. RNA samples were next denatured at 65 °C for 10 min followed by rapid cooling on ice for 5 min. Biotinylated RNA was separated from non-labelled RNA using Streptavidin Magnetic Beads (NEB). Beads (125 μl) were added to each sample and incubated for 15 min at room temperature, then washed with wash/binding buffer (0.5 M NaCl, 20 mM Tris-HCl and 1 mM EDTA) and low salt wash buffer (0.15 M NaCl, 20 mM Tris-HCl and 1 mM EDTA). 4sU-RNA was eluted from beads with 100 μl freshly prepared DTT buffer and incubate for 5 min. The pre-existing RNA and newly transcribed RNA were recovered by ethanol precipitation at -80 °C for 1hr. RNA was collected with centrifugation at 20,000 ×g for 20 min at 4 °C and dissolved in RNase free water. Before the cDNA synthesis, unmodified control RNA (NEB) was added to each sample (0.013 pmol per sample) and reverse transcription was conducted. Then qPCR was performed to determine additional cycles.

The ratio between pre-existing and newly transcribed RNA k was estimated by

Please cite this article in press as: Liu et al., Tumors exploit FTO-mediated regulation of glycolytic metabolism to evade immune surveillance, Cell Metabolism (2021), https://doi.org/10.1016/j.cmet.2021.04.001

$$k = \frac{A_t,\ pre-existing \times A_0,\ newly-transcribed}{A_t,\ newly-transcribed \times A_0,\ pre-existing}$$

where t is 4sU incubation time (min), A_t and A_0 represent mRNA quantity at time t and time 0.

Expression and purification of FTO protein

The $FTO_{\Delta N31}$ gene was cloned into the pET28a vector and then transformed into *E. coli* BL21 (DE3) cells for expressing of His-tag fusion human FTO with N-terminal 31 residues truncated. The cells were cultured at 37 °C until A_{600} reached 0.6-0.8 and then the expression of FTO was induced by 0.5 mM Isopropyl β-D-Thiogalactopyranoside overnight at 16 °C. FTO was purified in turn by HisTrap HP column, MonoQ column and Superdex 200 (GE Healthcare). The purities of target proteins were checked by the 12% SDS-PAGE and protein concentration was determined by the absorbance at 280 nm.

Inhibition of Dac51 on FTO demethylation of m^{6}A-contianing RNA

The inhibitory activity of Dac51 on FTO was determined by a high-performance liquid chromatography (HPLC)-based assay according to the previously described methods (Huang et al., 2015, 2019b). 5.0 μM 15-mer ssRNA (5′-AUUGUCA(m^{6}A)CAGCAGC-3′, Genescript) was incubated with 0.3 μM FTO at room temperature for 3 hr in the buffer containing 280 μM $(NH_4)_2Fe(SO4)_2$, 2 mM L-ascorbic acid, 300 μM 2OG, and 50 mM Tris-HCl (pH 8.0), with various concentrations of Dac51. Then the reaction was quenched at 65 °C for 10 min. Then 300 μl anhydrous ethanol, 10 μl 3 M sodium acetate (pH 5.2), and 10 μl glycogen was added to 100 μl samples to precipitate the ssRNA at -80 °C overnight. The precipitation was collected by centrifugation and then subjected to digestion by nuclease P1 (Sigma) at 42 °C with 100 mM CH_3COONH_4 for 8 hr. Then the pH of the enzyme digestion system was adjusted to 9.0 with 2 M NH_4HCO_3 followed by digestion of alkaline phosphatase (Sigma). The amount of m^{6}A in the final products was quantified by HPLC (Agilent 1100) and the IC_{50} was calculated with GraphPad Prism 5.0 according to the inhibitory percentage on the demethylation of FTO under various concentrations of Dac51. All reactions were performed in triplicate.

Crystallization and structure determination of FTO-Dac51 complex

Crystals of FTO-Dac51 complex were obtained under the condition of 0.1 M sodium citrate (pH 5.8), 12% (w/v) polyethylene glycol (PEG) 3350, and 8% isopropanol in a hanging-drop vapor-diffusion method at 20 °C. Before subjected to diffraction, the crystals were cryo-protected using 20% (v/v) glycerol and flash-frozen in liquid nitrogen. Diffraction data were collected on the BL19U1 beamline at the Shanghai Synchrotron Research Facility (SSRF). After data processing within HKL2000, the structure of FTO-Dac51 was determined by molecular replacement using the FTO/MA complex structure (PDB: 4QKN) as search model. The structural model of FTO-Dac51 complex was built using COOT and computational refinement was performed in REFMAC5.

Cellular Thermal Shift Assay (CESTA)

This assay was performed according to the previously described protocol (Martinez Molina et al., 2013). 1.5 × 10^7 B16-OVA or LLC cells were collected, washed with ice-cold 1 × PBS and subjected to freeze-thaw cycles with liquid nitrogen in the lysis buffer (50 mM Tris-HCl (pH 7.5), 150 mM NaCl, and 2 mM DTT) plus protease inhibitor cocktail. After centrifugation, the supernatant was incubated with various concentrations of Dac51 for 25 min and then transferred into the PCR tubes followed by denaturing at indicated temperatures for 3 min. Then the samples were centrifuged, and the supernatant was analyzed by western blotting assay with the FTO antibody (Abcam), β-Actin antibody (Proteintech), HRP-conjugated goat anti-rabbit IgG (Cwbio) and HRP-conjugated goat anti-mouse IgG (Cwbio).

Cell treatment

For Dac51 treatment, 5 × 10^5 B16-OVA cells were treated with Dac51 at a final concentration of 1 μM or 5 μM for 48 hr. For IFN-γ treatment, 1 × 10^6 B16-OVA cells were treated with 5 or 10 ng/ml IFN-γ for 16 hr. For oligomycin treatment, 1 × 10^5 B16-OVA cells in the 96-well cell culture plate were treated with 2 μM oligomycin for 6 hr.

Sample process and organoid culture

Dissociated tumor cells were collected in Advanced DMEM/F12 (Thermo Fisher), suspended in growth factor reduced (GFR) matrigel (Corning). The matrigel was then solidified and overlaid with 500 μl of complete human organoid medium, which was subsequently refreshed every two days until passage. Patient-derived organoids (PDOs) were cultured in Advanced DMEM/F12, supplemented with 1 × B27 additive and 1 × N2 additive (Thermo Fisher), 0.01% bovine serum albumin, 2 mM L-glutamine, 100 units/ml penicillin-streptomycin, and containing the following additives: EGF, Noggin, R-spondin 1, [Leu15]-Gastrin I, FGF-10, FGF-basic, Wnt-3A, Y-27632, Nicotinamide, A83-01, SB202190, HGF (PEPROTECH). The colorectal cancer organoids were done following the method as previously described (Yin et al., 2020).

Drug treatment and Peripheral Blood Mononuclear Cells (PBMC) co-culture

Organoids were harvested and washed with PBS. TrypLE (Invitrogen) was added to resuspend the organoids and these were digested for 10 min at 37 °C. Subsequently, organoids were mechanically dissociated by pipetting, resuspended in 5% Matrigel

complete growth medium before plating in 50 μl volumes detached 96-well plate. After 30 min at 37 °C, additional 100 μl organoids complete growth medium was added. Dac51 were added 2 days after plating, 15 μl of each 10 × Dac51 stock solution was added. After 10 μM Dac51 treatment for 48hr, the pairs of matched PBMC from NSCLC patients were co-culture with NSCLC organoids at a ratio of 10:1 for 24 hr. IFN-γ production in the supernatant of the culture medium was detected by IFN-γ Flex set CBA assay (BD).

General methods for synthesis of compounds

All solvents and reagents were purchased from commercial sources and used as received. ^{1}H NMR, ^{19}F NMR, and ^{13}C NMR spectra were recorded with a Varian-MERCURY Plus-400, BRUKER 500, or BRUKER 600 NMR spectrometer at room temperature. NMR spectra were calibrated to the solvent signals of deuterated DMSO-d_6 or $CDCl_3$. Chemical shifts are reported in ppm (δ scale) as referenced to TMS and coupling constant (J) values are reported in hertz (Hz). Data are presented as follows: chemical shift, multiplicity (s = singlet, d = doublet, dd = doublet of doublet, t = triplet, q = quartet, m = multiplet, br = broad), coupling constant, and integration. Low-resolution electrospray ionization mass spectrometry (LRESI) was recorded on a Finnigan LCQ/DECA spectrometer, and high-resolution electrospray ionization mass spectrometry (HRESI) was recorded on a Micromass Ultra Q-TOF spectrometer. Flash column chromatography was performed using silica gel (230-400 mesh). Reverse phase flash column chromatography was run on LISURE Science EZ PLUS 100D instrument. Analytical TLC was performed on silica gel plates and visualized under ultraviolet light at a wavelength of 254 nm.

Synthesis of the FTO inhibitor Dac51

The synthetic route was shown in Figure S5A. Compounds **3** and **4** were synthesized according to the previously reported synthetic route (Huang et al., 2019b).

Compound 3. ^{1}H NMR (400 MHz, DMSO-d_6) δ 13.20 (s, 1H), 9.47 (s, 1H), 7.92 - 8.00 (2H), 7.90 (m, 1H), 7.33 (t, J = 7.8 Hz, 1H), 6.81 (t, J = 7.2 Hz, 1H), 6.25 (dd, J = 7.2, 2.8 Hz, 1H). ^{13}C NMR (126 MHz, DMSO-d_6) δ 170.43, 147.09, 137.49, 135.36, 135.09, 134.91, 134.67, 132.01, 119.49, 118.21, 113.60, 112.53.

Compound 4. ^{1}H NMR (400 MHz, $CDCl_3$) δ 9.40 (s, 1H), 8.04 (d, J = 8.0 Hz, 1H), 7.60 - 7.77 (2H), 7.36 - 7.25 (m, 1H), 6.82 (t, J = 7.6 Hz, 1H), 6.36 (m, 1H), 4.42 (q, J = 7.2 Hz, 2H), 1.45 (t, J = 7.8 Hz, 3H). ^{13}C NMR (126 MHz, $CDCl_3$) δ 168.53, 146.73, 137.21, 134.92, 134.74, 134.57, 133.88, 131.48, 118.74, 117.90, 113.76, 112.31, 60.84, 14.34.

Compound 6. The mixture of compound **4** (3.43 g, 8.8 mmol), 3,5-dimethyl-4-(4,4,5,5-tetramethyl-1,3,2-dioxaborolan-2-yl)-1H-pyrazole 5 (2.94 g, 13.2 mmol), anhydrous K_2CO_3 (2.43 g, 17.6 mmol), Pd(dppf)Cl_2 (646 mg, 0.88 mmol) in co-solvents of 1,4-dioxane and water (88 ml, 10:1 (v:v)) was stirred at 100 °C for 24 hr under N_2 atmosphere. The reaction mixture was evaporated and subjected flash column chromatography with silica gel, which provided compound **6** as a white solid (2.16 g, 40% yield). ^{1}H NMR (500 MHz, DMSO-d_6) δ 9.29 (s, 1H), 7.94 (dd, J = 8.0, 1.6 Hz, 1H), 7.60 (s, 2H), 7.45-7.37 (m, 1H), 6.88-6.81 (m, 1H), 6.40-6.31 (m, 1H), 4.37 (q, J = 7.1 Hz, 2H), 2.34 (s, 6H), 1.37 (t, J = 7.1 Hz, 3H). ^{13}C NMR (126 MHz, DMSO-d_6) δ 167.75, 146.87, 141.70, 134.50, 133.49, 132.90, 132.60, 131.08, 129.11, 117.75, 115.29, 113.51, 111.33, 60.75, 14.16, 10.80. LRESI m/z (% relative abundance) 404.2 ([M+H]$^+$, 100); HRESI m/z calcd for $C_{20}H_20Cl_2N_3O_2$ [M+H]$^+$ 404.0933, found 404.0927.

Compound 7. To an ice-cooled solution of compound **6** (1.8 g, 4.46 mmol) in THF (8 ml) and EtOH (16 ml) was added a solution of LiOH (535 mg, 22.3 mmol) in water (4 ml) slowly. Then the reaction mixture was stirred at 45 °C overnight. After complete consumption of compound **6** monitored by TLC, the reaction mixture was concentrated under vacuum. The residue was re-dissolved in water (4 ml) and acidified to pH 3.0 by aqueous HCl (2.0 M). After filtration, the cake was washed with water (5 ml) and dried to give compound **7** as a white solid (1.1 g, 65% yield). ^{1}H NMR (600 MHz, DMSO-d_6) δ 12.62 (s, 1H), 10.01 (s, 1H), 7.92 (s, 1H), 7.57 (s, 1H), 7.49 (s, 2H), 7.30 (s, 1H), 6.76 (s, 1H), 6.30 (s, 1H), 2.26 (s, 6H). ^{13}C NMR (126 MHz, DMSO-d_6) δ 170.00, 147.27, 141.12, 134.22, 133.36, 132.18, 131.48, 128.69, 117.41, 114.38, 113.15, 111.80, 11.29. LRESI m/z (% relative abundance) 376.2 ([M+H]$^+$, 100); HRESI m/z calcd for $C_{18}H_{16}Cl_2N_3O_2$ [M+H]$^+$ 376.0620, found 376.0620.

Dac51. A solution of compound **7** (1.1 g, 3.0 mmol), O-(tetrahydro-2H-pyran-2-yl)hydroxylamine (527 mg, 4.5 mmol), EDCI (692 mg, 3.6 mmol), HOBT·H_2O (551 mg, 3.6 mmol) in anhydrous DMF (15 ml) was stirred at room temperature for 24 hr. Fifteen ml water was added and off-white solid appeared immediately. The solid **8** (1.1 g) was collected by filtration and dried under vacuum. Compound **8** was used directly in the next step without purification. To a solution of compound **8** (1.19 g, 2.5 mmol) in cosolvents of MeOH and DCM (8 ml, 1:1 (v:v)) was added TFA (5.7 g, 50 mmol) at room temperature. The obtained mixture was stirred overnight, and off-white precipitate appeared after the reaction completed. Target compound **Dac51** was obtained as TFA salt (967 mg, 64% yield) after filtration. ^{1}H NMR (500 MHz, DMSO-d_6) δ 11.33 (s, 1H), 9.49 (s, 1H), 7.54 (d, J = 7.6 Hz, 1H), 7.50 (s, 2H), 7.27 (t, J = 7.6 Hz, 1H), 6.79 (t, J = 7.4 Hz, 1H), 6.34 (d, J = 8.2 Hz, 1H), 2.28 (s, 6H). ^{13}C NMR (126 MHz, DMSO-d_6) δ 166.94, 145.15, 141.67, 133.41, 133.38, 132.65, 132.19, 129.29, 128.26, 118.29, 115.82, 115.11, 114.07, 11.67. ^{19}F NMR (376 MHz, DMSO-d_6) δ -74.77. LRESI m/z (% relative abundance) 391.1 ([M+H]$^+$, 100); HRESI m/z calcd for $C_{18}H_{17}Cl_2N_4O_2$ [M+H]$^+$ 391.0729, found 391.0723.

TCGA data analysis

TCGAbiolinks v2.14.1 was used to download HTSeq counts matrix of RNA-seq and clinical information of solid tumors in TCGA through GDC portal (Colaprico et al., 2016). ENSEMBL ID was mapped to gene symbol with AnnotationDbi R package. For multiple-to-one mapping, the highest value was retained. Gene expression was further normalized to TPM value based on sequencing depth and the longest transcript length. Only genes with a transcript length of more than 150 bp were included, and only genes

Please cite this article in press as: Liu et al., Tumors exploit FTO-mediated regulation of glycolytic metabolism to evade immune surveillance, Cell Metabolism (2021), https://doi.org/10.1016/j.cmet.2021.04.001

with an average expression of at least 1 TPM were applied to downstream analysis. The estimation on immune components of TCGA tumor samples was downloaded from TIMER. TCGA tumor samples were then split into three groups according to their predicted $CD8^+$ T cell infiltration levels by TIMER based on the quartile threshold (Li et al., 2017a). The "CD8 high group" was considered as inflamed tumors and was used to investigate the potential regulators on CD8 cytotoxicity. The cytotoxic T lymphocyte (CTL) score was defined as the average expression of five reported signature genes (*CD8A*, *CD8B*, *GZMA*, *GZMB* and *PRF1*) to reflect the cytotoxicity of tumor-infiltrating T cells. For AML cancer in Table S1, we selected AML samples with relatively high signals of T cell signatures (exceeding upper quantile) based on the estimation by CIBERSORT and then performed correlation analysis (Newman et al., 2015). The survival R package was used for survival analysis, and survminer R package was used for visualization. Potential regulators associated with $CD8^+$ cytotoxicity T lymphocyte level were identified by calculating pairwise Spearman correction. One outlier of samples was removed for visualization but included in calculating the correlation in Figure 1B.

RNA-seq data analysis

Quality control on raw sequencing reads was performed by FastQC v0.11.8 (https://www.bioinformatics.babraham.ac.uk/projects/fastqc/). Adaptor and low quality bases were trimmed by Trim Galore! version 0.6.0, a wrapper tool around Cutadapt and FastQC with command "trim_galore -q 20 –three_prime_clip_R1 3 –clip_R2 3 –phred33 –illumina –stringency 3 –paired –length 36" (Martin, 2011). Ribosomal RNA was removed by Bowtie2 version 2.3.5 and reads that did not align concordantly were retained and applied to quality control again with FastQC (Langmead and Salzberg, 2012). Clean reads were then aligned to mm10 mouse genome with STAR version 2.7.0f in default setting (Dobin et al., 2013). Only alignments with mapping quality more than 20 were used for downstream analysis. Aligned reads were converted into bigwig format based on BPM normalization in 1 bp bin size with deepTools and visualized with Integrative Genomics Viewer (IGV) (Ramirez et al., 2014; Robinson et al., 2011). The featureCounts function of Rsubread v2.0.1 was utilized to count gene expression on transcriptome (Liao et al., 2014). Note that DNA contaminant was found in RNA-seq reads of co-cultured T cell samples, and this was corrected by subtracting the reads aligned to the reverse strand on exons. TPM normalization was performed as described above. Differential expressed analysis was performed by DESeq2 v1.26.0 (Love et al., 2014). Only genes with an average expression of at least 1 read among all samples were retained. Differentially expressed genes were defined as genes with adjust $p \leq 0.01$ and $|\log_2(\text{fold change})| \geq 0.5$.

ATAC-seq data analysis

Quality control on raw sequencing reads was performed by FastQC v0.11.8. Adaptor and low-quality bases were trimmed by Trim Galore! version 0.6.0 with command "trim_galore -q 20 –phred33 –nextera –stringency 3 –paired". Clean reads were then aligned to mm10 genome by Bowtie2 version 2.3.5 with parameter "-X 2000 –no-mixed –no-discordant" and alignments with mapping quality more than 20 were retained. Picard toolkit (http://broadinstitute.github.io/picard/) was used to remove duplicates and reads mapped to blacklist regions were discarded (Amemiya et al., 2019). Fragments below 100 bp were considered as originated from nucleosome-free regions and retained for downstream analysis (Buenrostro et al., 2013). Reads were then converted into bigwig format based on BPM normalization in 1 bp bin size with deepTools and visualized with IGV. MACS2 v2.1.3 was applied to call peak with parameter "-g mm –nomodel –shift -100 –extsize 200 -f BAM –keep-dup all" (Zhang et al., 2008). Diffbind v2.14.0 was used to merge ATAC-seq peaks to identify consensus peaks and perform differential accessibility analysis (Ross-Innes et al., 2012). Differential ATAC-seq peaks were defined as peaks with an absolute value in "Fold" column more than 0.5 and FDR less than 0.01. Motif enrichment analysis was performed by HOMER (Heinz et al., 2010). In brief, the binding motifs of transcription factors based on ChIP-seq experiments were downloaded from ChIPBase database (Zhou et al., 2017), and were utilized as known motif set for HOMER. To link the regulatory elements with target genes, Activity-by-contact model was utilized to infer to potential enhancer-promoter regulation and to calculate the regulation strength of each enhancer-promoter pair based on the ATAC-seq and H3K27ac ChIP-seq signal intensity (as well as genomic distance) (Fulco et al., 2019). The predicted regulation strength was multiplied by $\log_2$(fold change) of accessibility to measure the potential effect on expression, termed 'accessibility effect'. By adding up the accessibility effect on each gene from corresponding regulatory elements, the regulated genes were divided into two groups, "ATAC up" and "ATAC down".

Public ChIP-seq data analysis

The H3K27ac ChIP-seq of mouse melanoma was downloaded from GSE129621 (GSM2698555, GSM2698556) for re-analysis (Laurette et al., 2020). Quality control on raw sequencing reads was performed by FastQC v0.11.8. Bowtie version 1.2.2 with parameter "-p 20 -m 1 –strata –best -y –sam -l 40" was used to align single-end reads to mm10 mouse genome (Langmead et al., 2009). Only alignments with mapping quality more than 20 were retained. MACS2 v2.1.3 was applied to call peak with parameter "–nomodel -f BAM -g mm" (Zhang et al., 2008). The public ChIP-seq peaks of c-Jun, JunB, and C/EBPβ was downloaded from ChIP-Atlas database and converted to mm10 genome coordinates with LiftOver (Haeussler et al., 2019; Oki et al., 2018).

m^6A-seq data analysis

Basic sequencing quality control, sequence alignment, and visualization were performed as described in RNA-seq data analysis. m^6A peaks were called by exomePeak v2.16.0, and 100 bp sequences around peak center were extracted for motif enrichment with HOMER (Heinz et al., 2010; Meng et al., 2013). Metagene distributions of both m^6A reads and m^6A peaks were analyzed with custom R script. In brief, the genomic coordinates of read/peak center were compared with 5'UTR/CDS/3'UTR annotation of gene models to define the relative position of each read/peak. m^6A methylation ratio was defined as the normalized CPM value of

IP reads within the m^{6}A peaks divided by the TPM value of the given gene. Differential methylated genes were considered as genes with at least one differential m^{6}A peak, which was defined as an m^{6}A peak with a difference on m^{6}A methylation ratio larger than 0.5.

Functional enrichment analysis

For mouse co-culture RNA-seq data, clusterProfiler v3.14.3 was employed to compute enrichment scores on CD8$^+$ T effector markers from previous literature (Pace et al., 2018). For shNC or sh*Fto*-1 B16-OVA RNA-seq, functional enrichment analysis was performed on mouse hallmark gene sets downloaded from http://bioinf.wehi.edu.au/software/MSigDB/ (The last version of 11 October 2016) by clusterProfiler v3.14.3 (Yu et al., 2012). For FTO-m^{6}A direct-regulated genes, the GO terms of molecular function from MSigDB database were tested for enrichment (Subramanian et al., 2005).

QUANTIFICATION AND STATISTICAL ANALYSIS

Statistical analysis was done using GraphPad Prism 7.0. For comparison of two groups, two-tailed unpaired Student's t tests or Mann-Whitney U tests were performed. For comparison of more than two groups, one-way ANOVA comparisons tests were performed. For Kaplan-Meier survival curves, the *p* values were calculated using the log-rank test. Data are shown as mean ± SEM. and statistical significance was denoted with *($p < 0.05$), **($p < 0.01$), and ***($p < 0.001$) in the figures. Experiments were repeated two to three times.